

FORCE STUDIES OF INTRACELLULAR TRANSPORT

BY

BENJAMIN HENRY BLEHM

DISSERTATION

Submitted in partial fulfillment of the requirements  
for the degree of Doctor of Philosophy in Physics  
in the Graduate College of the  
University of Illinois at Urbana-Champaign, 2012

Urbana, Illinois

Doctoral Committee:

Professor Taekjip Ha, Chair  
Paul R. Selvin, Director of Research  
Professor Brian DeMarco  
Professor Yoshitsugu Oono

## ABSTRACT

Cytoskeletal motors like kinesin-1 and dynein are necessary for intracellular transport and a variety of other functions in the cell. They have been well characterized in simplified, single-motor, *in vitro* systems, but less is known about their mechanical properties *in vivo*, in a more complex, multi-motor environment. In order to better study these properties and their impact on intracellular transport, we have built an optical trap to implement a recently developed theoretical technique which allows us to calibrate and measure forces in a living cell and other viscoelastic environments. We have found that lipid droplets in A549 cells and phagocytosed beads in *Dictyostelium* cells typically have 1 active plus-end directed motor and 1 active minus-end directed motor. Also, the plus-end motor's stall force appears to be lower (2-3 pN) than kinesin-1's *in vitro* stall force (5-7 pN), while the minus-end motor's stall force (2 pN) is slightly higher but similar to many *in vitro* measurements of dynein's stall force. Stall force measurements made *in vitro* by measuring the stall force of beads with both kinesin and dynein attached give results similar to those *in vivo*, supporting a synergistic transport model, in which dynein remains attached to the microtubule at all times, being dragged behind the kinesin and reducing its stall force when the cargo is moving in the plus direction, and being the sole active motor when the cargo is moving in the negative direction.

## **Acknowledgements**

I would like thank my advisor Dr. Paul Selvin, coadvisor Dr. Yann Chemla, Dr. Matt Comstock and my labmates for all the help and advice.

The project described herein was supported by NIH Grant R01 AR44420 and NSF Grant DBI 06-49779. Its contents are solely the responsibility of the authors and do not necessarily represent the views of the NIH or NSF.

# Table of Contents

<b>Chapter 1: Introduction</b>	<b>1</b>
<b>Chapter 2: Materials and Methods</b>	<b>23</b>
<b>Chapter 3: Results</b>	<b>53</b>
<b>Chapter 4: Discussion</b>	<b>63</b>
<b>Chapter 5: Conclusion</b>	<b>71</b>
<b>References</b>	<b>73</b>
<b>Appendix</b>	<b>76</b>

# Chapter 1: Introduction

Herein I will present data on the measurement of cytoskeletal motor stall forces *in vivo*. This section will introduce the cytoskeletal motors involved, the basics of optical trapping, and the differences between the *in vitro* and the *in vivo* environment.

## Section 1.1: Cytoskeletal Motors

Cytoskeletal motors are a type of molecular motor that walk along the cellular cytoskeleton. Molecular motors convert chemical energy, typically in the form of ATP (Adenosine TriPhosphate) into mechanical energy, which in the case of cytoskeletal motors translocates them along the cytoskeletal track they are using. There many types of cytoskeletal motors, grouped into the Kinesins, Dyneins, and Myosins. The Kinesins and Dyneins walk along microtubules, while the Myosins walk along actin filaments[1, 2]. Microtubules are long, tube-like protein polymers made up of dimers of alpha and beta tubulin. The tubulin sticks together to form filaments, and then the filaments group together (typically in groups of 13) to form a microtubule. Sets of microtubules can also stick together to form axonemes, which kinesin and dynein will also walk along (Fig 1). They are polarized with the minus ends of the microtubules typically at the centrosome near the nucleus and the plus ends extending outward towards the cell periphery. Actin is also a protein polymer made up of actin monomers, and is arrayed more randomly throughout the cell. In this work we will be mainly concerned with the microtubule-based motors conventional kinesin (kinesin-1), and cytoplasmic dynein.

Using single molecule fluorescence techniques and optical trapping, the stepping rate, size, and force have been measured for a variety of motors *in vitro*. Kinesin-1 walks in the plus

direction, has an 8 nm step size and an *in vitro* stall force of 5-7 pN, where stall force is the backward force required to stop a motor, and the step size is the distance the motor's tail region or center moves with every step forward[3-7]. Kinesin-1 is a homodimer of two kinesin heavy chains with a monomer consisting of a globular motor domain referred to as the "head" of the protein and a long alpha-helical tail region (Fig 2). The head is the region which binds the microtubule and contains the catalytic site that binds ATP. The tail consists of the lever arm region, which acts like a leg allowing kinesin to walk, a coiled-coil region where the two monomers wrap around each other to form a dimer, and a cargo binding domain. There can also be assorted light chains which aid in cargo binding.

Dynein is a much more complex motor than kinesin, being substantially larger, having more light and medium chains than kinesin, and exhibiting much higher variability in step size and direction. It is a negative end directed motor, and appears to have a step size of 8 nm and possibly multiples thereof[8]. Unlike kinesin, dynein also takes backwards (plus end directed) steps fairly often, especially under backward forces[9-11]. Its structure is very different from kinesin's, consisting of a homodimer with a microtubule binding domain on a stalk attached to a large circular ATPase region, with multiple ATPase sites, after which there is a coiled-coil region for dimerization and binding of a large array of light chains, intermediate chains, and cargo (Fig 3)[12]. Measurements for its *in vitro* stall force range from 1-7pN, with different constructs and purifications yielding very different results, although cytoplasmic dynein appears to typically have a stall force of 1-2 pN according to most measurements[8, 9]. Due to the fact that *in vitro* measurements remove dynein from possible secondary protein interactions occurring *in vivo*, it is possible that the lower stall force measurements are due to dynein lacking parts of its structure or cofactors necessary to its proper functioning[11].

Although myosin isn't the focus of this research it will be useful to note a few of its characteristics. Myosins are directional like kinesin and dynein, and all myosins except for myosin VI walk toward the plus end of actin. Many myosins aren't transport proteins like kinesin and dynein, instead playing roles in force generation in muscles and aiding endocytosis. Myosin V, a typical transport myosin, walks toward the plus end of actin, has a 36nm step, and a stall force of around 3 pN [13, 14]. It is structured similar to kinesin, being a homodimer with a motor domain that contains the actin binding and ATPase sites and a tail region consisting of a leg (substantially longer than kinesin's, explaining its larger step size), coiled-coil region where the monomers bind together, and a cargo binding domain (Fig 4). Myosin VI has a similar structure, step size and stall force, but walks in the opposite direction on actin[15].

## **Section 1.2: Optical Trap**

Optical traps are instruments that allow one to measure and exert force at the microscopic and nanoscopic scale. They typically consist of a laser focused to a point through a microscope's objective lens. Particles are drawn to the center of this focus due to radiation pressure from index of refraction differences between the particles and the surrounding media. Optical traps can be used to measure particle position relative to the trap center and with a calibrated trap can be used to measure the force on a particle in the trap[16].

One way optical traps can be used to measure distance is by imaging the back focal plane of the microscope condenser[17]. This method allows one to detect particle movement relative to the laser but not laser movement by itself. This happens because the condenser is one focal length away from its back focal plane, which maps the laser translation in the focal plane to laser angle changes in the back focal plane, and angle changes in the focal plane to laser translations in

the back focal plane (Fig 5). Another lens then takes the back focal plane as its object and maps it to an image plane that is on a QPD (Quadrant PhotoDiode) according to the thin lens formula:

$$\frac{1}{f} = \frac{1}{I} + \frac{1}{O}, \quad (1)$$

where  $f$  is the focal length of the lens,  $I$  is the distance to the image from the lens and  $O$  is the distance to the object from the lens. The QPD is simply four diodes arranged in a quadrant that detect the amount of light impinging on each diode. Subtracting the amount of light on the top half from the amount of light on the bottom half allows one to get position in one dimension, while the other dimension is obtained by subtracting the left from the right. The reason we only see particle movements relative to the laser and not laser movements in themselves, is that particle movements relative to the laser refract the laser, causing the laser's angle to change, which is mapped to a translation at the QPD, while laser movements at the sample plane are mapped to angle changes at the QPD which the QPD will not pick up.

The basic theory behind the trap's ability to exert force can be looked at in two different ways depending upon the size of the particles being trapped relative to the wavelength of the trapping laser [16, 18]. For particles much larger than the wavelength of the trapping laser (in this case 1064 nm) simple ray optics can be used to explain the trapping force as seen in figure 6. When a bead is centered in the trap, the laser's refraction is equal and opposite on each side of the bead, and therefore there is no net force. However, if the bead is displaced to one side of the laser, then the refraction on one side is more intense than on the other, leading to a net change in momentum of the laser, which must be offset by an equal and opposite momentum change in the bead. The force is proportional to the laser intensity, as the total momentum change is proportional to the laser intensity. There is also an axial force when the bead is displaced from the focus along the laser's path of propagation. Part of the force is from light reflected off the

bead and the rest is a restoring force from the refraction of the laser by the bead such that when the bead is before the focus, the laser diverges more causing a forward force, and when the bead is beyond the focus, the laser diverges less, causing a backward force.

For particles much smaller than the trapping laser's wavelength, the trapped particle can be treated as a perfect dipole, and the force on it from the laser can be seen as an electromagnetic Lorentz force that is caused by the local gradient in the electric field. The Lorentz force is:

$$F = q[E + (V \times B)], \quad (2)$$

where  $q$  is the charge of the particle,  $E$  is the electric field,  $V$  is the velocity, and  $B$  is the magnetic field. In this case the equation can be simplified down to:

$$F = \frac{a}{2} \times \nabla(E^2), \quad (3)$$

where  $a$  is the polarizability of the trapped particle. This force is due to the particle becoming an induced dipole in the trap's electric field.

However, in most trapping situations, the particle is similar in size to the trapping laser's wavelength. This makes the theoretical description much more complex, but the general picture presented in the previous two regimes still holds. For small motions near the laser focus (in our case approximately 200 nm on either side of the focus), the force  $F$  on the particle in the trap is linear, and acts as a spring with:

$$F = kx, \quad (4)$$

where  $x$  is the particle position relative to the trap and  $k$  is the spring constant, which for a trap is referred to as the trap stiffness.

The trap stiffness can be found in a variety of ways, 2 of which will be explained in the materials and methods chapter. The simplest way is to use the equipartition method. This works in viscous media, and involves observing the variance of the trapped particle. Essentially, the

stronger the trap, the less the particle can move around, and the smaller the variance as seen in Eq. (5).

$$k = \frac{k_B T}{\langle x^2 \rangle}, \quad (5)$$

where  $k$  is the trap's stiffness,  $k_B$  is the Boltzmann constant,  $T$  is the temperature in kelvin, and  $\langle x^2 \rangle$  is the variance in the particle's position.

Two force measurements that will be of some interest in this discussion are the stall force and the detachment force. A stall force measurement is simply a measurement of how far a motor can move a cargo against the trapping laser until the motor can no longer move due to the trap's restoring force. This leads the motor to stall out against the trap, and stop moving, generally staying stuck in place for a period of time until the motor detaches and returns to the center of the trap. Detachment force is simply the force at which a motor detaches and falls back into the trap, with no required pause or stalling of the motor. Figure 7 shows a typical *in vitro* kinesin trace, where the kinesin is attached to a bead in an optical trap. There are many detachment events, and a few stall events, which is typical, as cytoskeletal motors typically detach much more often than they stall, because their detachment force is lower than their stall force. However stall events still occur as detachment is a stochastic process, and will occur even without a backward trapping force.

### **Section 1.3: *In Vitro* Versus *In Vivo***

Almost all cytoskeletal motor and optical trap measurements take place in an *in vitro* environment, typically a buffered solution around pH 7, with some salts, ATP, a single type of cytoskeletal track and a single type of motor. This homogeneous, controllable environment is very useful for measurement of purified, single-motor activities, but leaves many questions about

the protein-cellular environment interactions that occur in the cell. Unfortunately, the *in vivo* environment is not so homogeneous or controllable, presenting a much less tractable problem when attempting to observe and measure motor activities in their natural setting. Nonetheless, these measurements are necessary, as *in vivo* motors operate in a radically different environment than *in vitro* motors, with multiple motors, types of motors, accessory proteins, and cellular signals affecting their actions and behavior (figure 8). Not only are there more elaborate motor complexes, the cellular environment is also viscoelastic, causing not only viscous drag, but also elastic tethering to surrounding structures such as organelles and the cytoskeletal matrix[19, 20]. This mixture of spring-like elastic behavior and friction-like viscous behavior makes it impossible to calibrate the trap using older *in vitro* methods.

Previous attempts to measure forces *in vivo* have all involved making assumptions about the cargo to be trapped, such as cargo size, shape, local viscosity, and the invariance of all these characteristics, and then calibrating before or after the experiment in a similar *in vitro* environment (generally lacking any elastic component other than the trap)[18, 21, 22]. Even when some of these properties are measured directly, they are not constantly monitored throughout the experiment, even though the cargo and its cellular environment are variable in time, which leads to errors in force measurement and misses most of the interesting information about intracellular dynamics. A new method developed by the Berg-Sorensen lab, called the Fluctuation-Dissipation Theorem (FDT) method, can calibrate during an *in vivo* experiment where the viscous and elastic interactions between the object to be trapped and its environment are unknown[23, 24].

Most people think of viscosity and elasticity in separate situations: a viscous fluid like water or honey, or an elastic solid like a bouncy ball or a spring. In reality, everything is

viscoelastic, containing both viscous and elastic characteristics, it just so happens that in many situations one predominates. In a cell however, neither characteristic is predominant, leading to an environment with properties that are quite unusual to most people, and very different from the standard environment of the *in vitro* experiment. One of the primary differences is that in viscoelastic environments, the behavior of the local environment is dependent upon the size of the particle and the time scale of interest. Much of this behavior is from the intracellular polymers that abound in the cell, including microtubules, actin polymers and intermediate filaments (figure 9)[25]. These polymers have a characteristic mesh size that leads to particles larger than the mesh becoming elastically entangled in the mesh while smaller particles experience mainly viscous forces. However, at long time scales, these polymers can deform, which leads to viscous behavior for large particles, and smaller particles will diffuse into different areas of the mesh which act as elastic barriers to them. For smaller particles the mesh can be thought of as the rooms of a house, where for short distances and time scales, one freely moves around the room, but for longer timescales and distances one begins to run into the walls, which impedes one's ability to move freely. In this work the cell can be thought of as the house, and the cargos being transported by motor proteins are trying to move around the cell, between different rooms of the house.

## **Section 1.4: Intracellular Transport**

There are two broad types of intracellular transport: passive and active. Passive transport occurs through diffusion, does not require any energy input other than the surrounding heat bath, and is random. Molecules that are small, need to be evenly spaced around the cell, and aren't turned over too rapidly can be transported using this method. Active transport occurs through

some sort of energy-dependent mechanism and is directed. Cargoes that need to be concentrated differentially throughout the cell need to be transported with this method, as do cargoes that have to be transported long distances over short periods of time. The type of active transport we are interested in is intracellular cargo transport carried out by kinesin and dynein along microtubule filaments. The motors are the energy-dependent (ATP) active transporter, but how the transport is directed is an area of active research, with how different motors are activated and deactivated to determine directionality as an area of particular controversy.

A major question yet to be resolved is the role motor copy number plays in regulating intracellular motion. Intracellular cargo transport is typically bidirectional and saltatory, and how cargoes are directed and controlled is uncertain[26-28]. The fact that motion is saltatory with frequent pauses, velocity changes and directional reversals is puzzling. Is cargo directionality determined mainly by a tug of war between opposite directionality motors, or are motors coordinated, or do other regulatory factors play a large role? Currently it is thought that cargoes have both positive and negative direction microtubule motors, potentially with a myosin motor also attached. When one of the microtubule motors is knocked out, all cargoes typically carrying that motor stop in many situations, indicating that, at least for microtubule-based motion, both positive and negative end directed motors are frequently necessary[29, 30].

Two of the major models explaining intracellular organelle motility are the Tug-of-War (TW) and the Coordinated Switching (CS) model[26]. The TW model hypothesizes that cargo directionality is determined by teams of opposite directed motors in competition with no coordination outside of force transmission through the cargo and associated complexes. The teams of motors attach and detach depending on their individual characteristics and the net force upon them as seen in figure 10. In the most basic version of the model, one set of motors pulls

the other set off due to the ability to exert higher forces, either through a higher stall or detachment force per motor, or due to more motors. This leads to one set of motors dominating motion by pulling the weaker set of motors off, until the dominant set of motors changes, which can occur by stochastic motor-microtubule detachment and attachment events. The characteristics of the motors themselves (stall force, detachment force, on/off rate) and the number of motors are the sole determinants of direction.

The coordinated switching model posits that some external regulatory factor activates one set of motors or the other, so that they never are simultaneously active (fig 10). This model was widely favored until recently for several reasons: motors competing against each other would seem to be a waste of energy, it was thought that competing sets of motors would lead to cargos stalling out and not being able to move, and in many *in vivo* systems, if one motor is knocked out, motility completely stops. However rebuttals to many of these arguments have appeared recently. First, if motors were competing against each other, energy would be expended simply moving back and forth for no apparent reason. This would appear to be true, but it is known that intracellular transport is bidirectional and saltatory, so energy does appear to be expended simply moving back and forth. Second, competing teams of motors would appear to stall out if they had certain characteristics, but modeling and some *in vitro* experiments have shown that saltatory, long range bidirectional motion can occur with teams of motors with no external regulation. The modeling experiments show that this can occur if the motors have a specific set of characteristics, one of which is a detachment force lower than the stall force [31, 32]. Third, although many *in vivo* systems do show impaired motility in both directions if one motor is knocked out, *in vitro* experiments clearly do not show such impairment, implying that something in the *in vivo* environment is causing this impairment. Microtubule associated proteins and other

blockages on the cytoskeletal tracks or perhaps other regulatory mechanism could be causing this[33]. Also, some *in vivo* systems do not show impaired motility in both directions if one motor is knocked out [34]. In these systems, instead of the removal of a motor causing motility to completely stop, cargos accumulate at the end of the microtubules (the end to which the remaining motor is directed).

Other interesting *in vivo* measurements are the stall forces of dynein and kinesin, one of the major questions of the molecular motor field today. As discussed previously, for dynein this is a fairly controversial question in the cytoskeletal motor field, and is particularly interesting in light of the two models of intracellular transport and kinesin's measured *in vitro* stall force. Compared to kinesin's *in vitro* stall force of 5-7 pN, dynein's 1-2 pN force is quite low, which leads to question of why it appears to be so much lower. One explanation is that the *in vivo* stall force of dynein and/or kinesin will be different due to motor complex components present in the cell that are not present in *in vitro* assays[11]. If this is not the case, the TW model would have to posit that there are significantly more dynein attached to cargo than kinesin, and even for the coordinated motion model, it would seem unusual that one direction of motion would require more force than the other.

## **Section 1.5: The Experiment**

The end result of the experiments described herein is the measurement of stall force and motor copy number *in vivo*. The experiments first involved testing the new trap calibration method *in vitro*. This consisted of creating viscoelastic environments and then measuring the viscoelasticity of the environment using the FDT method and comparing to previous

measurements of the environment. We then looked at the effect of viscoelasticity on stall force in this *in vitro* environment.

After that, stall forces of organelles *in vivo* were measured. As the directionality of microtubules *in vivo* is generally plus end toward the cell membrane, we split the stalls into plus or minus-end directed based on whether they were headed towards or away from the membrane (anterograde or retrograde). This allowed us to measure the stall forces of what are presumably kinesin and dynein. Then, due to the additive nature of stall forces, we determined motor copy number by comparing the stall force measured to the lowest stall force peak. If we measure a stall force of 6 pN and the lowest peak in that direction is 2 pN, presumably that organelle had 3 motors of that directionality on it that were active simultaneously.

The *in vivo* systems that we use, A549 cells and *Dictyostelium discoideum*, were chosen for ease of use in that they had vesicles which could be trapped and were highly motile. A549 cells are human lung epithelial tissue cells, and contain a large number of lipid droplets that range from 200 nm up to 1  $\mu\text{m}$  in diameter. They are known to use kinesin-1 and cytoplasmic dynein in vesicular transport, although the motors on the lipid droplets themselves haven't been directly studied[22]. *Dictyostelium discoideum* is a slime mold that exists unicellularly in a nutrient rich environment, but as soon as crowding or a lack of food occurs can form aggregates, either slugs or a fruiting body that will release spores. They eat bacteria in the wild, through phagocytosis, but in the lab can be grown axenically, on media. We grew them on *E. coli*, and fed them polystyrene beads to form trappable phagosomes. *Dictyostelium* are a well characterized model organism used to study phagocytosis and other cellular processes, and a variety of evidence points to a kinesin, DdUnc104, which is a relative of unc104 in *C. elegans*, as

the plus end directed motor, and cytoplasmic dynein as the minus end directed motor in these cells [35-37].

The final set of experiments, which we are currently in the middle of, is purifying the organelles that were trapped *in vivo*, reconstituting their motility *in vitro*, and measuring their stall forces. This is necessary to determine if the stall forces measured *in vivo* are significantly changed due to their *in vivo* environment or due solely to the motors' inherent properties.

*In vivo* and *in vitro* stall force measurements have been previously made on various organelles: *Dictyostelium* endosomes, A549 lipid droplets, mitochondria in *Reticulomyxa*, and lipid droplets in *Drosophila* embryos. However, none of these experiments have used a trap that is accurately calibrated *in vivo* to measure organelle stall forces, nor have they compared the *in vivo* values to the *in vitro* stall forces of the same organelles. The stall force values for the different *in vivo* measurements differ significantly, with kinesin measurements of 2 pN or 4-7 pN and dynein measurements of 2 pN, 4 pN, or 7 pN and the lack of comparison between the organelles in different cells and between *in vivo* and purified organelles *in vitro* leave the issue of whether these measurements are broadly applicable and whether there is something special about the organelles or cells that leads to differing behaviors *in vivo* and *in vitro* [21, 22, 38, 39].

## Section 1.6: Figures

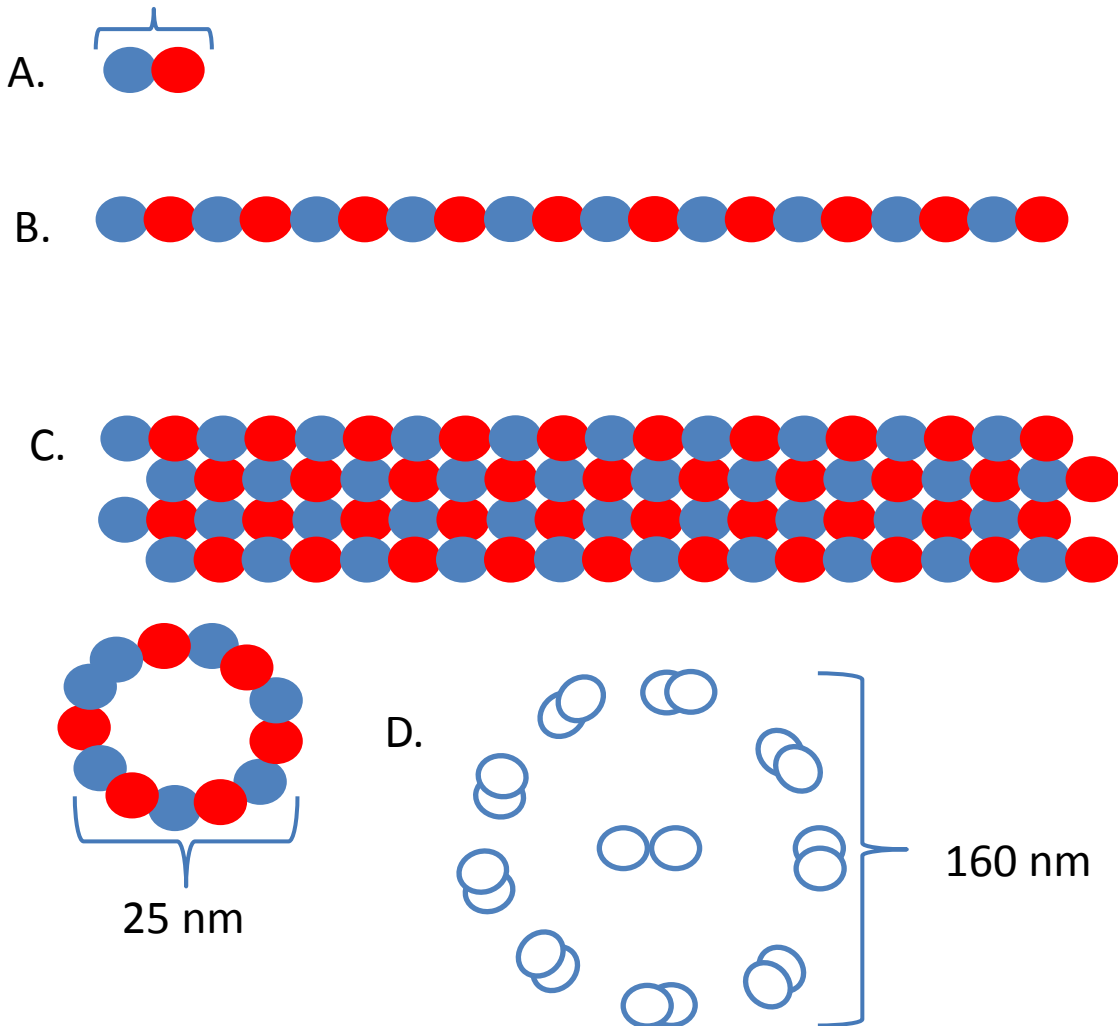


Figure 1: Microtubule Structure. A. A tubulin dimer consisting of an alpha and a beta tubulin. B. A protofilament made up of tubulin dimers. C. A microtubule viewed from the side and head on. Microtubules are typically made up of 13 protofilaments. D. An axoneme, with the circles representing microtubules. There are typically 9 sets of 1.5 microtubules along the outside and a pair of microtubules in the center of an axoneme, along with other binding and support proteins.

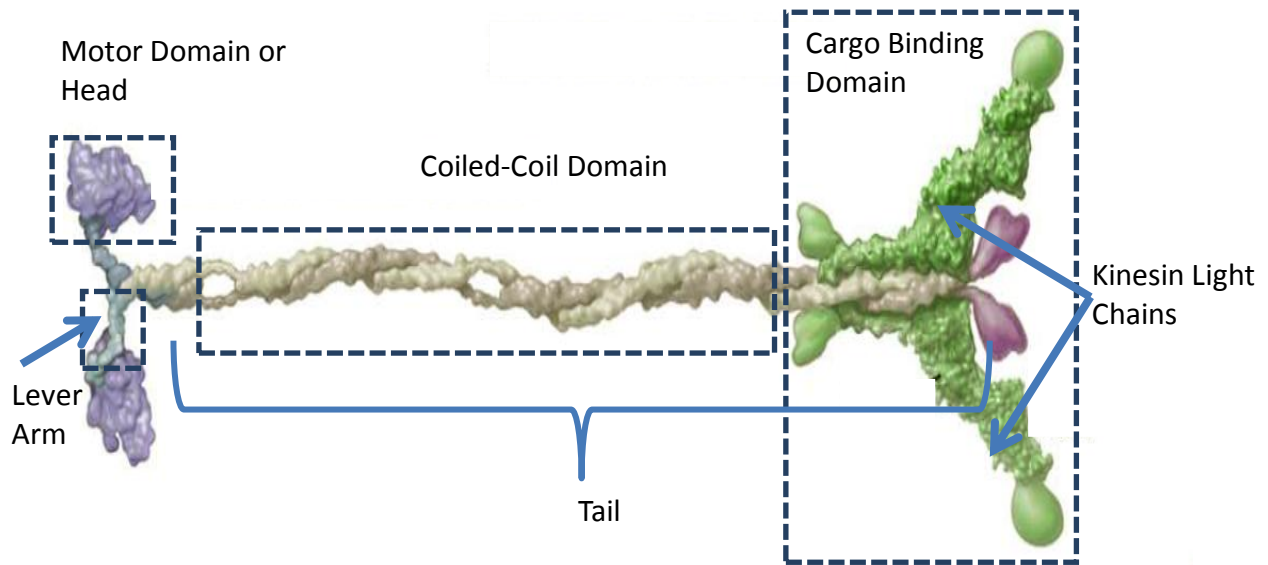


Figure 2: Kinesin-1's Structure: A kinesin-1 consisting of two heavy chains and two light chains is shown. Structural features such as the motor domain, coiled-coil region and cargo-binding domain are outlined. Figure used with permission from Vale 2003 [1].

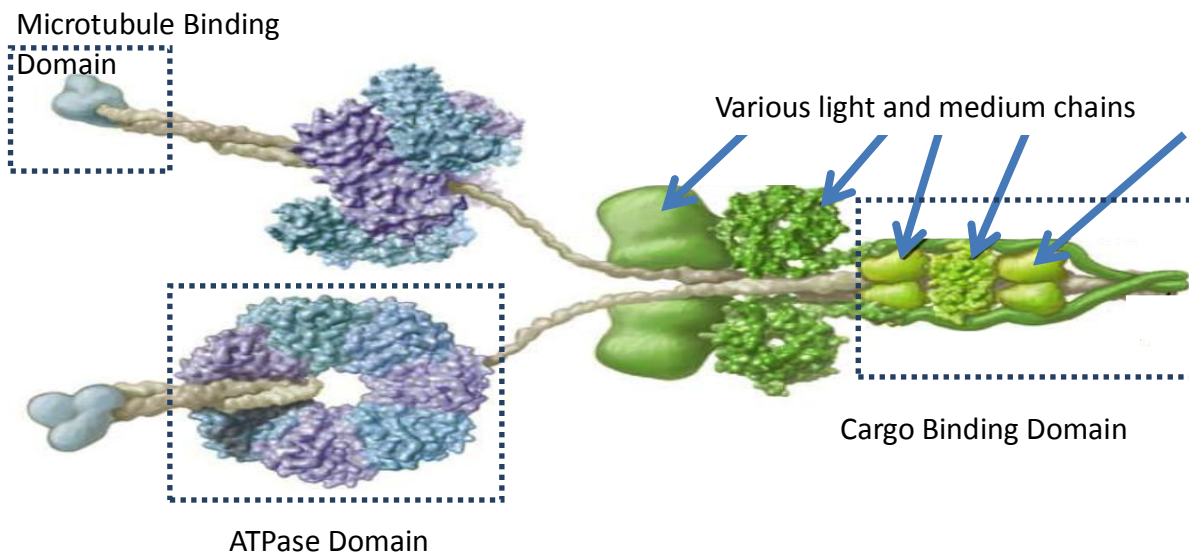


Figure 3: Cytoplasmic Dynein's Structure: A dynein consisting of two heavy chains and assorted light and intermediate chains is shown. Various structural regions are outlined, such as the microtubule binding domain at the end of the stalk, the ATPase domain, and the cargo binding domain. Figure used with permission from Vale 2003[1].

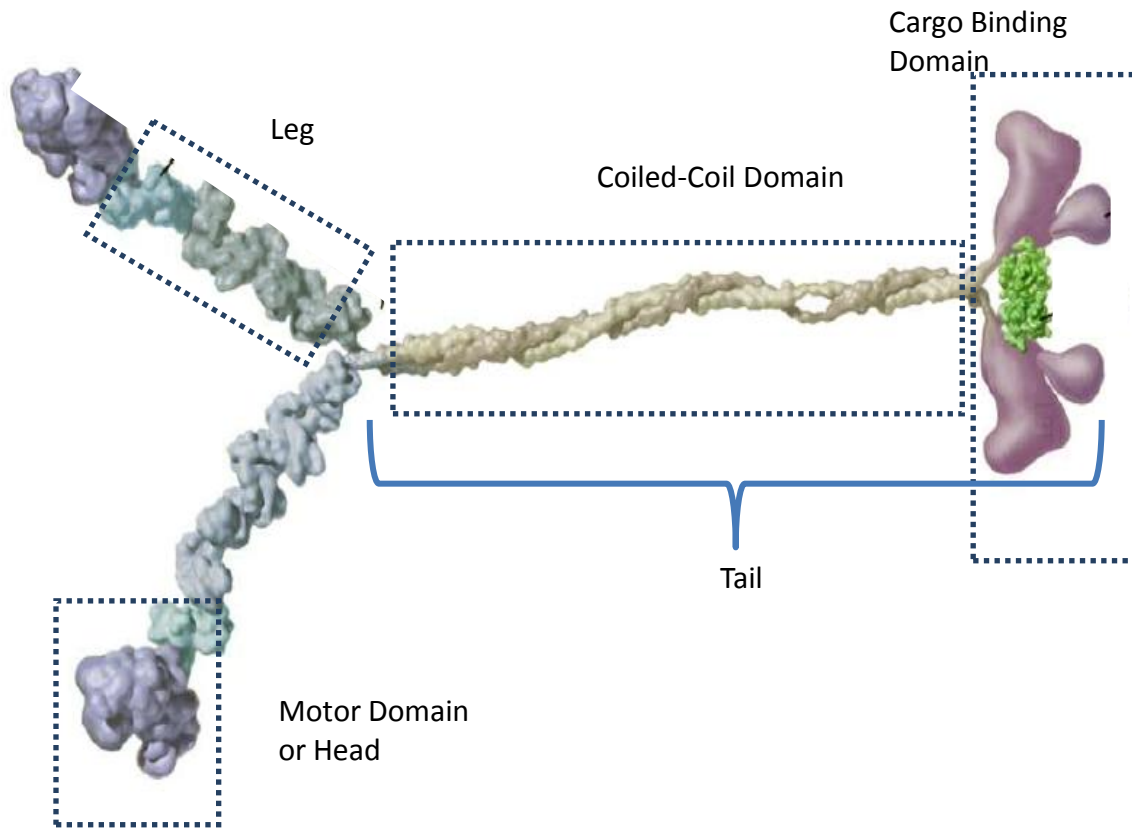


Figure 4: Myosin V's Structure: A myosin V made up of 2 heavy chains and various associated proteins. The heavy chain is made up of a motor domain, leg, coiled-coil and cargo-binding domain. Figure used with permission from Vale 2003[1].

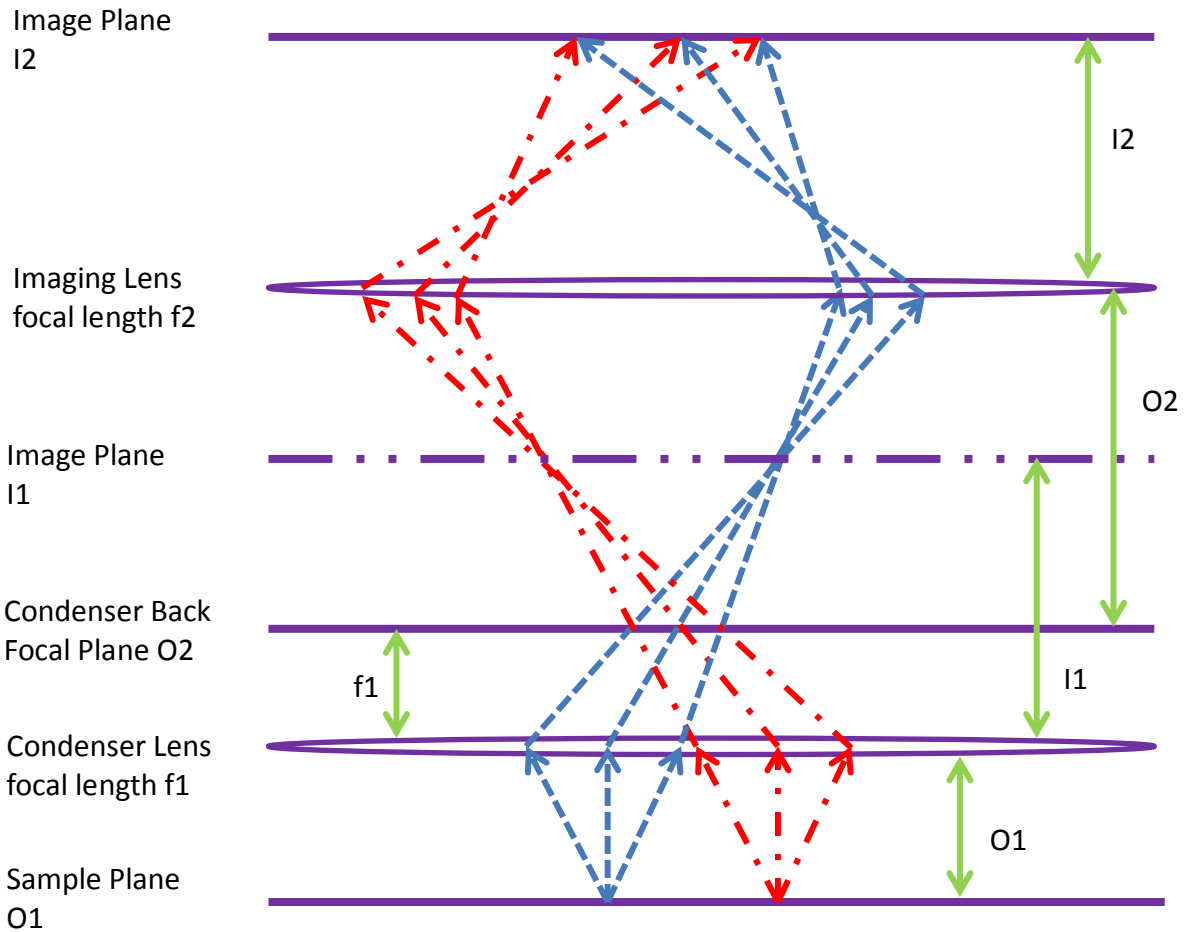


Figure 5: Back Focal Plane Position Detection: This diagram illustrates back focal plane imaging to map angular changes in the sample plane to movements at the QPD (imaging plane 2). O stands for object and I for image, as in object-image pairs for the thin lens formula, and  $f$  stands for focal length. If one follows the ray diagram, there are two separate points in the sample plane, each with light at different angles leaving it. That light is mapped to the back focal plane of the condenser such that a ray from any position at a specific angle is mapped to the same position in the bfp, but different positions at the sample plane just give different angles at the bfp. The condenser then images the sample plane at I1, but the lens after the condenser takes the bfp as its object, mapping it to image plane I2, where the QPD is placed. This leads to only angular changes in the sample plane being detected, and these angle changes are caused by the motion of the particle in the trap.

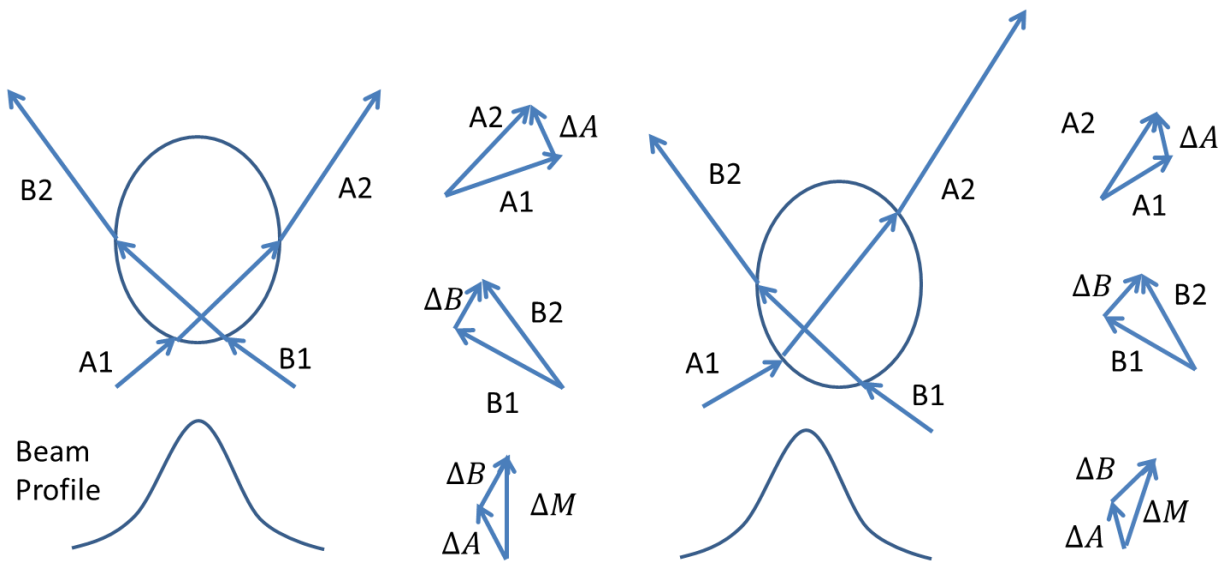


Figure 6: Optical Trapping Force Ray Diagram: This ray diagram shows a trapped particle in two conditions. The condition where the bead is centered in the trap is on the left, and the bead is off-center is to the right. In the leftmost diagram we see two rays entering the particle (A and B). After the rays have left the particle, their direction of propagation has changed, which means their momentum has changed. By mapping out their momentum change on the right of the bead, we can see that the net momentum change of both rays cancels out in the horizontal plane, but leaves a net change along the direction of propagation. This net momentum change can only be caused by an equal and opposite change in momentum of the bead, causing a net backward force on the bead, which offsets the force caused by the trapping beam partially reflecting off the bead. The right diagram shows a bead off-center in the trap, which leads to different levels of refraction for each beam. These momentum changes then add up to a net momentum change up and to the right. This causes an equal and opposite change in the bead, leading to a restoring force to the left and down on the bead, back into the center of the trap.

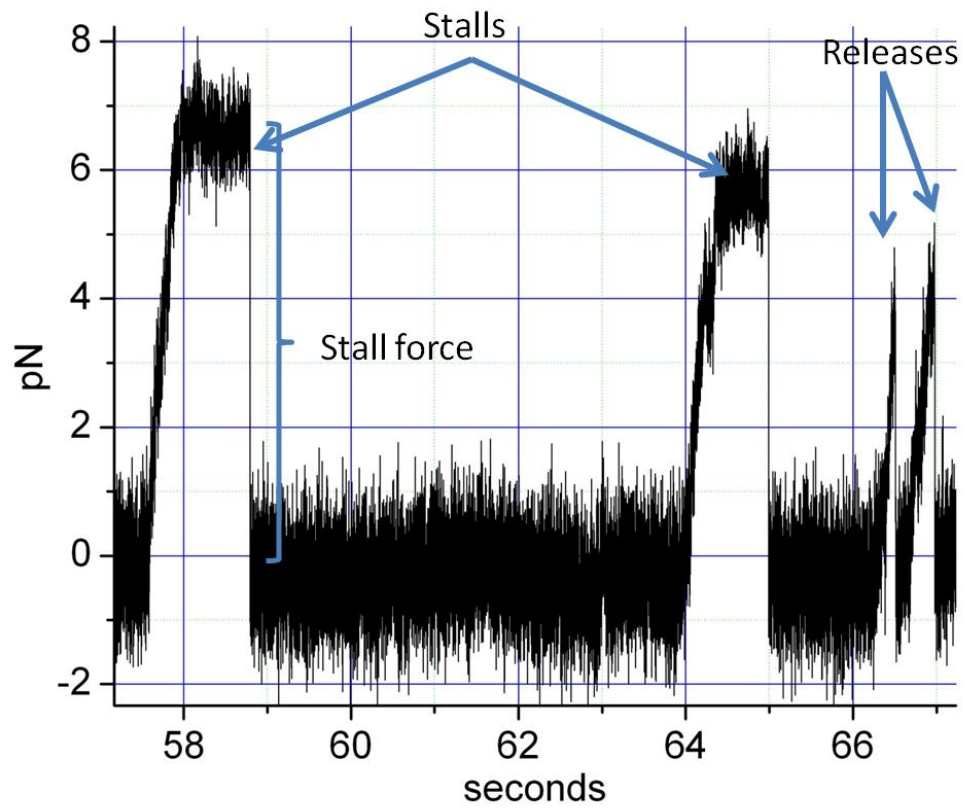


Figure 7: *In Vitro* Kinesin Stalls and Releases. This graph shows a typical position data trace for a kinesin coated bead *in vitro*, with 2 stall events and 2 release events.

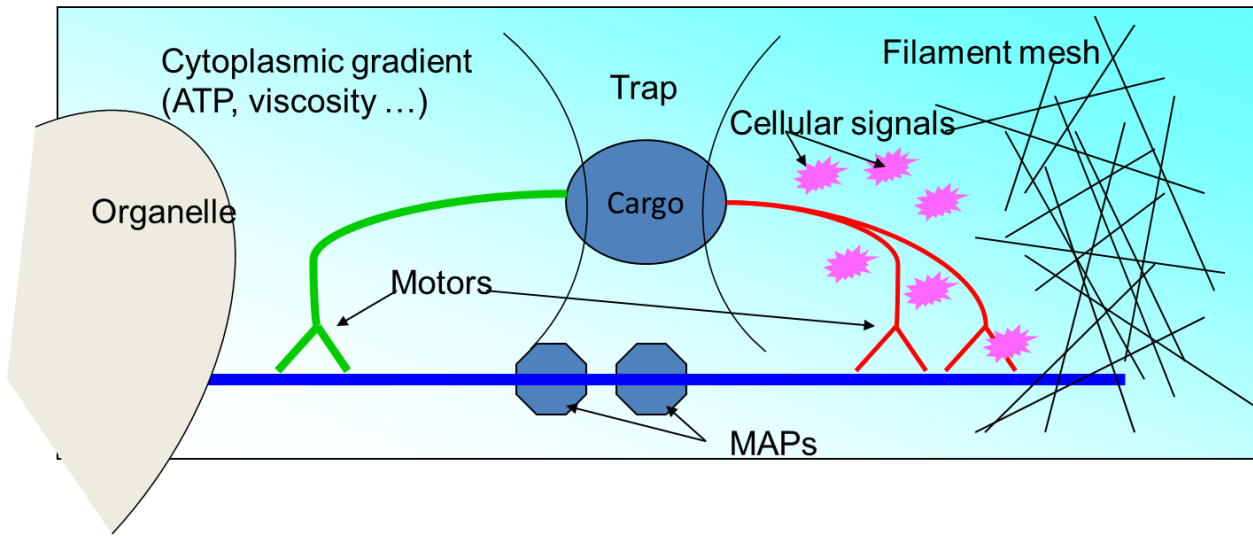
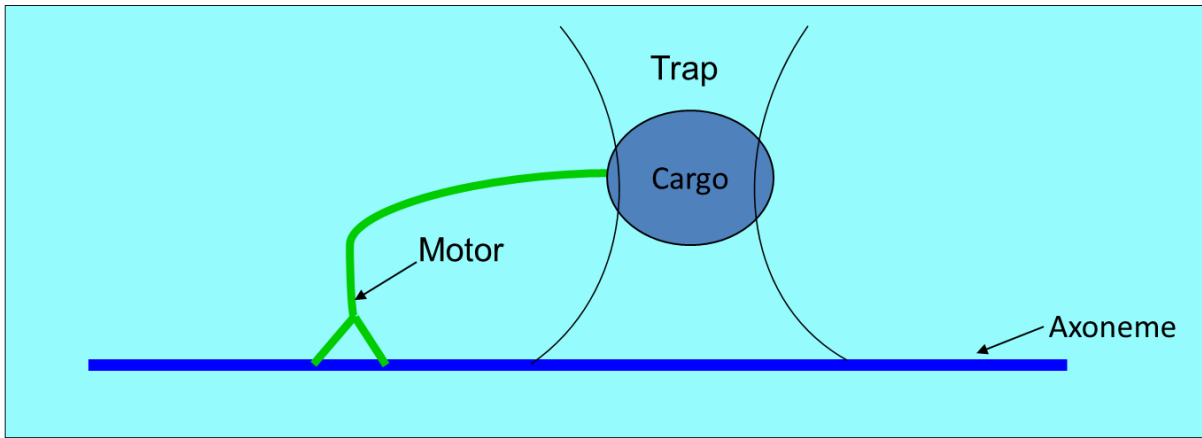


Figure 8: *In Vitro* vs *in Vivo* Environment: The top figure shows a typical *in vitro* experiment. There is a single motor type attached to a bead, walking along an axoneme in a viscous solution, containing mainly salts and ATP. The lower figure shows an example of a typical experiment *in vivo*. The cargo has multiple motors and motor types attached, there are environmental gradients of various molecules, proteins attached to the cytoskeletal track and organelles and filament meshes to run into. These experimental differences could lead to quite different outcomes.

	Example	Response Function
Viscous	water, glycerol	$F = \eta v$
Viscoelastic	amorphous polymers, silly putty	unknown, frequency and length scale dependent
Elastic	spring	$F = kx$

Viscoelastic components in the cell:

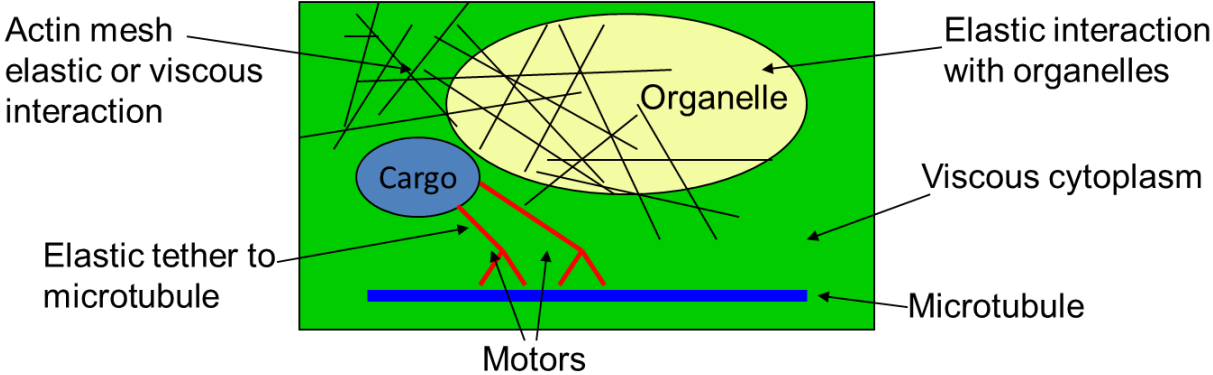


Figure 9: Viscoelasticity: Characteristics and Cellular Causes. The top table gives examples and response functions for various environments, while the bottom picture points out components of the cellular environment and how they interact with the trapped cargo.

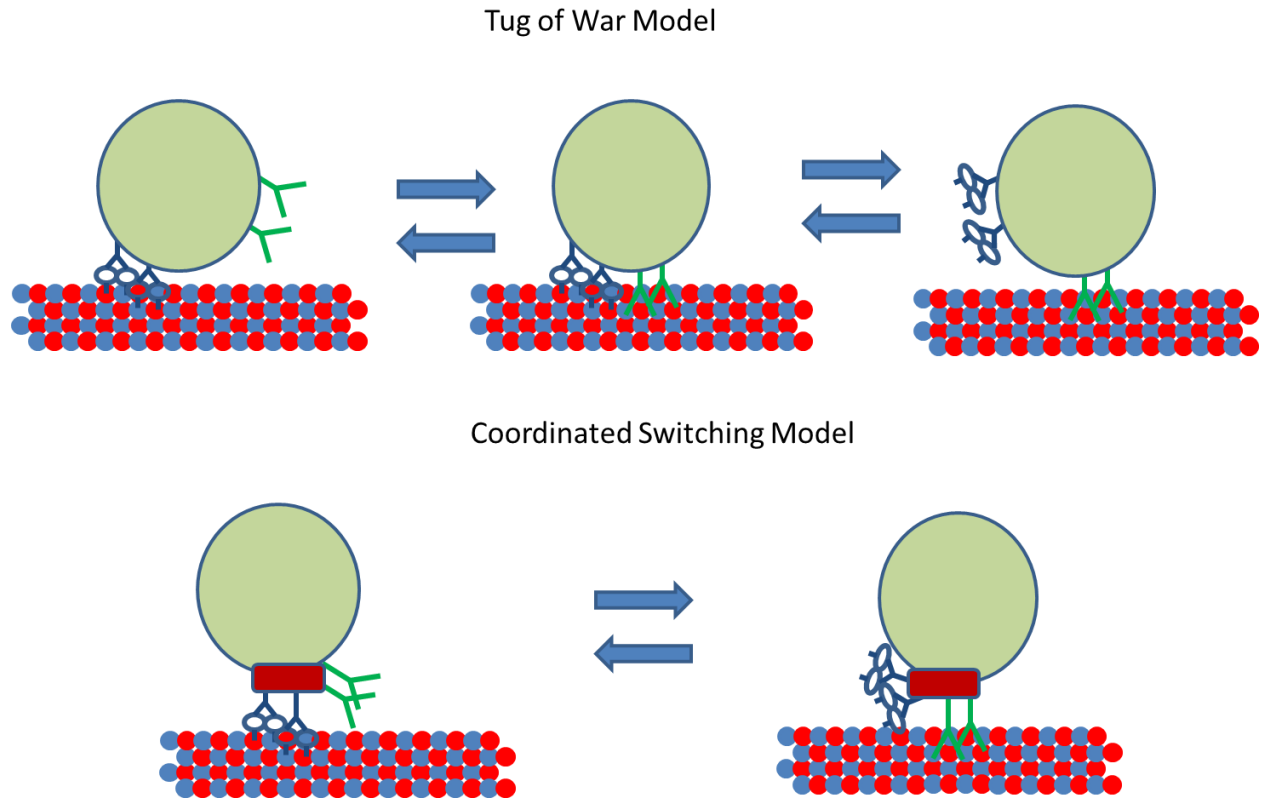


Figure 10: Intracellular Transport Models: These diagrams depict the different possible situations an organelle can be in according to a model. The tug of war model assumes essentially three different states. The center state where both teams of motors are attached and active, leading to a stall with no motion. The left state is where dynein has won the tug of war and kinesin has detached, leading to minus-end directed motion, the right state is where kinesin has won the tug of war, dynein has detached, and plus-end motion is occurring. The coordinated switching model has essentially two states. The left state is where the dynein are active, and kinesin are shut off, and the right state is the kinesin are active and the dynein are shut off. There is no state in which both types of motors are active simultaneously.

## Chapter 2: Materials & Methods

Care of biological samples, sample preparation, the optical trapping apparatus, experimental procedures, and data analysis are described in this chapter.

### Section 2.1: Biological Samples

#### Full Length Kinesin

Full length kinesin was obtained from the lab of Kathy Trybus, University of Vermont, and purified as described[40]:

The mouse kinesin KIF5B heavy chain (Invitrogen, accession number BC090841) and kinesin light chain 2 gene (ATCC, accession number BC014845) were used as polymerase chain reaction templates for insertion of the two clones into separate baculovirus transfer vectors (pAcSG2, BD Biosciences). The full-length kinesin heavy chain gene, and a truncated construct ending at amino acid 406 (kinesin-406), were cloned with a C-terminal hexa-HIS tag. A truncated version of the kinesin heavy chain (kinesin-C), ending at Ala<sup>888</sup>, was cloned with a C-terminal biotin tag for attachment to streptavidin Qdots, followed by a FLAG epitope to facilitate purification. The biotin tag is an 88 amino acid sequence segment from the Escherichia coli biotin carboxyl carrier protein, which is biotinized at a single lysine during expression in Sf9 cells [as described in (35) for myosin V]. The mouse kinesin light chain was cloned with yellow fluorescent protein (YFP) at the C-terminus. Recombinant baculovirus was prepared by standard protocols. Kinesin-406 was expressed in E. coli and purified on a nickel affinity column as described below, while all other constructs were expressed in Sf9 cells.

For full-length kinesin, Sf9 cells were co-infected with recombinant baculovirus coding for HIS-tagged kinesin heavy chain and YFP-tagged light chain, and grown in suspension for 72 h. Cells were sonicated in buffer containing 10 mM sodium phosphate, pH 7.5, 0.3 M NaCl, 0.5% glycerol, 7% sucrose, 2 mM  $\beta$ -mercaptoethanol, 0.5 mM AEBSF, 5  $\mu$ g/mL leupeptin, and 5 mM benzamidine. The cell lysate was clarified at 200,000  $\times$  g for 30 min, and the supernatant applied to a HIS-Select<sup>®</sup> nickel affinity column (Sigma–Aldrich) at a flow rate of 0.5 mL/min. The resin was washed first with buffer A (10 mM sodium phosphate, 10 mM imidazole, pH 7.5, 0.3M NaCl, 0.5 mM AEBSF, 5  $\mu$ g/mL leupeptin and 5 mM benzamidine), and then with buffer A containing 30 mM imidazole. Kinesin was eluted from the column with 10 mM sodium phosphate, 200 mM imidazole, pH 7.5, 0.3M NaCl and 1  $\mu$ g/mL leupeptin. The fractions of interest were combined and concentrated using an Amicon centrifugal filter device (Millipore), and dialyzed in 10 mM HEPES, pH 7.3, 200 mM NaCl, 50% glycerol, 1 mM DTT, 10  $\mu$ M MgATP and 1  $\mu$ g/mL leupeptin for storage at  $-20^{\circ}\text{C}$ .

#### Mammalian Dynein

Mammalian dynein from bovine brain was obtained from the lab of Trina Schroer, Johns Hopkins University and purified as described[41]:

Briefly, five bovine brains are homogenized and a cleared, high-speed supernatant is generated. This supernatant is loaded onto an SP-Sepahrose Fast Flow chromatography column and the .5 M KCl elution peak is layered onto sucrose cushions and centrifuged overnight. The next day, the sucrose cushions are recovered, loaded onto a second SP-Sepahrose Fast Flow column, and the .5 M KCl elution peak is layered onto sucrose gradients and centrifuged overnight. On the third day, the sucrose gradients are fractionated and the fractions are analyzed by sodium dodecyl sulfate-polyacrylamide gel electrophoresis (SDS-PAGE) to identify those fractions that contain predominantly dynactin polypeptides and a small number of contaminant polypeptides. These fractions are pooled and loaded onto a Mono Q column and the protein peaks are separated by ion-exchange chromatography...The first major peak, which contains cytoplasmic dynein (MQ dynein), elutes from the column at 320 mM KCl and corresponds to a little over three fractions.

## **Axonemes**

Axonemes were purified in lab from sea urchin (*Strongylocentrotus purpuratus*) sperm.

Sea urchins were obtained from Pt. Loma Marine Invertebrate Lab (11103 Highway 67 Lakeside, CA 92040) or Tom's Caribbean Tropicals ([www.divertom.com](http://www.divertom.com)), and were requested to be gravid to maximize the number that would release semen. As soon as the sea urchins arrived, they were placed in room temperature Instant Ocean (obtainable in most aquarium or pet stores), as this apparently revived many of them and appeared to increase output. The sea urchins were injected with a few mL of .5M KCl, generally injecting until backward pressure is felt on the syringe or some KCl is expelled from the sea urchin. They were then set on a tray, and watched to see if semen or eggs came out (they will come out of the top of the urchins). Generally only 50-70% of urchins will excrete anything and half of them are excreting eggs, which are useless for this assay. We find that approximately 40 total urchins gives enough males to make 100's of assays worth of axonemes. The urchins that excrete semen are rinsed with Instant Ocean, ending up with a dilution of the semen in Instant Ocean of about 3X. Solutions were maintained at 4C after this point. Throughout the assay it was necessary to be careful not to dounce too much with the dounce homogenizer, as this led to short, useless axonemes due to shearing. The rest of this assay is taken from[42]:

1. Centrifuge at 2000g for 5 min to pellet sperm.

2. Resuspend by douncing the pellet in the same volume of buffer 1 (5mM imidazole: Cl<sup>-</sup>, pH 7.0, 100mM NaCl, 4mM MgSO<sub>4</sub>, 1mM CaCl<sub>2</sub>, .1 mM EDTA, .1mM ATP, 7mM 2ME) with 1% Triton X-100. Centrifuge at 1500g for 5 min (to pellet sperm heads). Centrifuge the supernatant at 12000g for 5 min.
3. Repeat step 4.
4. Resuspend the pellet by gently douncing in buffer 1. Centrifuge at 12,000g for 5 min. Repeat.
5. Resuspend the pellet by gently douncing in buffer 2(5mM imidazole:Cl<sup>-</sup>, pH 7.0, 600mM NaCl, 4mM MgSO<sub>4</sub>, 1mM CaCl<sub>2</sub>, .1mM EDTA, 7mM 2ME, 1mM DTT). Incubate for 10min, then centrifuge at 12,000g for 5 min.
6. Repeat step 7, but add 1% Triton X-100 to buffer 2 and raise the pH to 8.0.
7. Repeat step 6 with one added resuspension and centrifugation (total of 3).
8. Resuspend pellet in one-fifth volume of buffer 1 containing 50% v/v glycerol. Store at -20C.

## Section 2.2: The Optical Trap

Figures 11 and 12 are diagrams of the optical trap described here. The trap has an 1064 nm Nd:YVO<sub>4</sub> laser as the main trapping laser, with a 845 nm diode detection laser. Both lasers are then sent through optical isolators to reduce backscattering into the lasing cavity, which can have negative effects on the laser. The trapping beam then travels through a half wave plate and a polarizing beam splitter cube which are used to modulate the laser intensity. Two lenses then follow to collimate the beam, after which it travels through another half wave plate and polarizing beam splitter cube. An AOM (Acousto-Optic Modulator) for beam steering and a polarizing beam combining cube follow. Two lens telescopes follow, which serve to expand the beam, to steer the beams, and to map the image of the AOM onto the back focal plane of the microscope objective. The detection laser path goes through an optical isolator, neutral density filter to reduce its intensity to the point where it has negligible trapping effects at the sample plane, and a half wave plate and then goes through its own AOM for beam steering. After that there is a lens telescope, mapping the detection laser's AOM to the same plane as the trapping laser's AOM, and then a dichroic mirror which combines the detection laser (reflected) and the trapping laser (transmitted). The combined beams are then directed into an inverted microscope, with a 60X 1.2NA (Numerical Aperture) water objective, and a .9NA water condenser, after

which they are imaged onto a QPD such that the back focal plane of the condenser is mapped onto the QPD. A CCD camera is also used as a secondary detection device to image the sample plane and see the trapped particle's surrounding environment. There is also a 3D piezo stage that is used for fine sample positioning and a servo-motor stage for course adjustment. The data acquisition software and hardware used are Labview 8.6 and a National Instruments DAQ card.

#### Part descriptions:

Trapping Laser: 5W, BL-106C, power supply: J series J2OI-8S-12K-NSI Spectra-Physics

Detection Laser: 845 nm laser module Lumics LU0845M150-1G36F10A, fiber-Bragg grating stabilized.

Detection Laser Power and Temperature Controller: Thorlabs LM14S2, TED200C, LDC205C

Optical Isolator 1064: Thorlabs IO-3-1064-HP

Optical Isolator 835: Thorlabs IO-3D-830-VLP

Acousto Optic Modulator: Gooch & Housego AOM 23080-3-1.06

Microscope: Nikon Eclipse TE2000-U

Objective: Nikon Apo VC 60x/1.2 WI inf/.15-.18 WD .27, Nikon Plan

Condenser: Nikon WI .9

QPD: Pacific Silicon Sensor, QP154-Q-HVSD (IR enhanced, high voltage bias) or low bias QP154-Q-T01032 (QPD), QP-SD2 PCB (sum-difference board on which it is mounted)

QPD Amplifier: Low noise low power amplifier, Mouser 595-INA217AIP

CCD Camera: Andor Ixon DV887DCS-BV

Halogen Lamp: Optical Analysis Corp 20500/34

Piezo Stage: XY stage is MCL 01069, Z stage is MCL 01166, controller is NanoDrive MCL 01312, Mad City Labs Inc, Madison, WI

Servo Motor Stage: MS-2000 XYZ automated stage and controller, Applied Scientific Imaging, [www.asiimaging.com](http://www.asiimaging.com)

Dichroics: 1: Chroma, beam combiner Z830 DCMV2 2: 800 DCSX, Chroma 3: special order from Chroma, no part number, transmits 460-750, reflects 850-1080, laser grade substrate, with antireflection coating

Half Wave Plates: Thorlabs

Polarizing Beam Splitter Cubes: Thorlabs

Rotation Controller: Newport ESP300, universal motion controller driver

Rotary Mount: Newport SR50PP

Lenses: Thorlabs, anti-reflection coating C, 1050-1620nm.

DAQ card: National Instruments PXI-7851R

Radio Frequency Generation Card: Analog Devices AD9852/PCBZ, ask for a RF digital synthesizer evaluation board.

RF oscillator: 14 pin DIP TCXO 30MHz, Connor Winfield HTFL-5A-030.00MHz

RF Amplifier: Minicircuits TIA-1000-1R8

DC Power Supplies: Acopian TD15-40

Cables: Standard BNC from ECE storeroom and shielded cables from MiniCircuits CBL-15FT-SMSM+

Software Control: Labview 8.6

Battery Backups and Surge Protectors: Isobar ultra TrippLite, and APC Back UPS XS1300.

Floated Optical Table: Newport RS-4000, Stabilizer I-2000 series legs

### **Polarizing Beam Splitter Cubes**

The trapping laser is sent through the first polarizing beam splitter cube to control the laser intensity by splitting off a portion of the laser light and sending it to a beam dump. This is necessary as decreasing the power to the laser changes the diameter of the beam coming out of the laser head, which adds a confounding factor when attempting to control the trap laser's stiffness. Therefore the laser is kept at full amplitude, and the intensity is controlled at the polarizing beam-splitter cube. The second pair of beam splitter cubes is used to set up a pair of optical traps. As we do not use dual traps in this experiment, the second trap has no impact on these experiments.

### **Battery Backups and Surge Protectors**

All sensitive electronics, especially laser diodes, always received power from a source twice removed from the wall socket AC. The building power was first sent through a surge protector and then through a combination battery backup and surge protector that had current conditioning (it could keep the current steady through brown outs and surges). This was necessary due to the fact that the building AC is unstable, and destroyed several detection laser diodes along with other equipment. The recommended battery backup and surge protector combination solution was received from Dr. Brian DeMarco's lab, which had experienced similar problems. It is important to note that a battery backup or surge protector alone will not

provide adequate protection from Loomis Lab's electrical fluctuations, and that the backups and surge protectors used in this setup are recommended as the minimum to ensure sufficient protection.

### **Acousto Optic Modulator**

The AOMs in our setup are used to steer the beam, and consist of a material, typically glass, attached to a transducer that sets up RF (radio frequency) acoustic waves in the crystal. These waves set up a diffraction grating, the spacing of which depends on the wavelength of the acoustic wave. Sending a laser through the AOM causes it to diffract into 0<sup>th</sup>, 1<sup>st</sup>, 2<sup>nd</sup>, and higher order beams. The AOM is typically constructed so that after careful alignment the majority of the laser will be diffracted into the 1<sup>st</sup> order beam. The amount of the beam diffracted into the 1<sup>st</sup> order is generally around 50% although most companies claim higher values, typically 80%. Since the amount the 1<sup>st</sup> order beam is diffracted depends upon the wavelength of the acoustic wave set up in the crystal, one can steer the beam by sending in different RF frequencies. The entire beam steering system consists of the DAQ card which controls the RF generating card, which then sends an RF signal to the RF amplifiers, which send the final amplified RF signal to the AOM.

An AOM is used to steer the beam for several reasons. The reason to use Acousto Optics is for the speed. The AOM can oscillate the beam on the order of  $\mu\text{sec}$ , and this limitation comes from the speed that a new acoustic wave can travel across the crystal. High frequency oscillations are necessary to avoid cellular processes and noise that occur at lower frequencies. We originally used an Acousto Optic Deflector, which is similar to an AOM, but has a larger range of diffraction, but there was a serious issue with it in that the AOD introduced noise on the order of nanometers in oscillations on the order of 10's of nanometers. This noise generated

extra peaks in the Fourier spectrum at multiples of the base oscillation frequency. It is possible to cut them out in the analysis after acquisition, and to reduce their size by decreasing the magnification of the image of the AOD, but these two solutions turned out to be unsatisfactory. Other labs have tried mapping out the noise to see if it is repeatable, but we found that this was also not satisfactory as the noise drifted over time[16, 43]. Dr. Comstock, from Dr. Yann Chemla's lab, discovered that AOMs still introduce this noise but at a rate more than an order of magnitude lower, and could still steer the beam in the sample plane over 1  $\mu\text{m}$ . The reduced noise is thought to occur because the different ways the transducers that generate the acoustic waves are set up in the AOM and AOD.

Unfortunately, even with the AOM there are still substantial peaks in the Fourier transform of the position data when oscillating the trap with an AOM. We discovered that this was due to the fact that the AOM was distorting the trap beam, but that this distortion had negligible effects on the actual position of the trapped particle. However the distortion had a noticeable effect when the beam was expanded, with a visible grating-like image overlaid on the beam. The effect was much worse for the AOD, but still present for the AOM. As the beam is partially expanded when it hits the QPD, the QPD picks up the movement of the overlaid distortion relative to the beam. To remove this effect we installed a detection laser to track the trapped particle's position. The detection beam is stationary while the trapping beam oscillates and therefore the detection beam completely removes the noise, as the noise was entirely due to distortion of the trapping beam.

## **Noise Control**

A wide variety of noise issues came up during the construction of the trap. The first set of issues came from the building power supply and the DC power supplies we used. These

issues were rectified by having the trap room's wiring checked and fixed, by using the surge protector/battery backup combination we use, and finally by making sure we had appropriately grounded most of the equipment. We had initially tried to use standard variable DC power supplies to power our QPDs and other instruments, but these introduced large amounts of noise. This situation was resolved by using higher quality Acopian power supplies. The last electronic noise issue we ran into was pickup through our QPD amplifiers, and through the cables that attached the RF generator to the RF amplifiers. These problems were resolved by buying highly shielded cables from Minicircuits and by putting the homemade amplifier circuits in a foam box covered in aluminum foil.

The other major noise issue we had was mechanical vibrations. These were from a wide array of sources as the trap was in an open area with other equipment and noise sources. The fiber optic cable for the detection laser was a major noise source as any movement caused fluctuations in its power and position, and the fiber was so light that the weakest air current would disturb it. The fiber was clamped to a table and put in a box, which mostly resolved the issue. All cables coming onto the floated optical table were clamped to the table with vibration damping foam (Lowe's Hardware) clamped around them.

Another basic issue involved stabilizing the microscope, particularly the condenser tower and the objective holder. We received drawings for modifications to the microscope from Dr. Matthew Lang, but the essence of the modifications was to stabilize the condenser and prevent the objective from moving, while simultaneously adding a dichroic below the objective to couple the trap and detection laser into the microscope[44]. This was done by adding extra mass and support to the microscope tower, adding mass and widening the microscope stage to allow more attachments, and by removing the objective turret from the microscope and mounting the

objective and dichroic in solid, immobile supports. Also, most microscopes come mounted on four rubber legs. These legs are not stable, and should be replaced with thick posts that can be clamped to the optical table.

Since many of the instruments used on the trap have cooling fans and most of them are near the trap (only the trapping laser power supply is in a different room, due to the fact that its fan is extremely loud and noisy), it is necessary to reduce the vibration they cause. All instruments with fans are mounted off the optical table on vibration damping foam. In some cases it has been useful to put sandbags on some of them to damp more of the vibrations. Ceiling air vents are another source of noise in Loomis Lab, and in the trap room covering the ceiling vent with a thin cloth filter and then surrounding it with a curtain significantly reduced air currents and noise. A cardboard box around the optics leading into the trap was also quite helpful, although we didn't completely enclose the trap. An accelerometer is extremely useful to measure the noise frequencies emitted by different equipment and measure what changes help or hinder noise reduction.

### **Software and Hardware Control**

Everything in the setup not controlled manually is controlled through a PXI-7851R DAQ card, mainly for the extremely accurate timing it allows in control and data acquisition. The reason this card has such good timing is due to the fact that it has a Field Programmable Gate Array (FPGA) and an extremely accurate clock. An FPGA is essentially a chip with gates that can be modified by the user, and part of the programming is actually on the card, thereby reducing the amount the computer and card have to communicate. Communication between the card and computer adds a significant amount of lag and uncertainty to control and data acquisition, so the FPGA improves timing accuracy. With older DAQ cards, trigger signals and

data acquisition could be off by tens to hundreds of  $\mu\text{sec}$ , while now timing is accurate to better than a single  $\mu\text{sec}$ . This was particularly important for measuring the relative phase of kHz oscillations. An offset of several  $\mu\text{sec}$  would render the relative phase measurement incorrect by several degrees, which would have a serious impact on the experimental analysis.

The other controller cards were two RF generating cards for the two AOMs. These cards, controlled by digital signals from the DAQ card, generate the FM RF signals that control the beam steering. They were obtained as test cards from Analog Devices. Their output runs through RF amplifiers to meet the wattage requirements of the AOMs, and prior to the amplifiers, runs through high pass RF filters (10MHz) to remove any potential negative effects low frequencies would have on the high frequency amplifiers.

The software for data acquisition and control was all run in Labview. There are two layers of Labview control, the programs that were loaded onto the FPGA card, and then the programs that controlled the FPGA card from the computer. Attaching these programs in an appendix is infeasible due to the fact the programming language is image based, but the project containing all of the programs can be obtained by emailing a request for them to [blehm@illinois.edu](mailto:blehm@illinois.edu).

### **Section 2.3: Trap Calibration**

We use two different methods to calibrate our trap's stiffness ( $k$ ), and two different methods to calibrate our volts to nanometers conversion for our QPD ( $\beta$ ). The power spectrum calibration method takes position data on the particle in the trap for a period of time while oscillating the trap's position sinusoidally at one frequency. The oscillation is to calibrate the  $\beta$  while a fit to the power spectrum of the position data, excluding the oscillation peak,

determines  $k$ . This technique assumes a viscous environment, but makes no assumptions about the local viscosity, and it is generally used to calibrate before or after actual experimental data is taken [45, 46].

The second calibration technique, the Fluctuation Dissipation Theorem (FDT) method, has three parts: the positional calibration to obtain  $\beta$ , and the active calibration and the passive calibration, which are used to determine  $k$ . The active calibration involves oscillating the trap at many different sinusoidal frequencies simultaneously and the passive simply observes the trapped particle. This technique has no assumptions about the environment's viscoelasticity, so it will work in a viscoelastic environment, and is typically carried out during the actual experimental data acquisition. Repeated short term calibrations are necessary, as in a living cell the trapped particle and environment can change in the course of the experiment. The fundamental requirements for this technique are that the trapped particle's oscillations are of the same order of magnitude as natural Brownian fluctuations, and that the local environment is homogeneous [23, 24].

### **Power Spectrum Calibration**

This calibration method is used mainly for our *in vitro* assays, and as a check against the FDT method when it is used *in vitro*. Experimentally, this technique is carried out by taking 8 half second sets of position data with the trap oscillating at 100 Hz. The power spectrum of each set of data is taken, and then the 8 power spectrums are averaged to reduce noise. The power spectrum is then fit with a Lorentzian and a delta-function spike at the oscillation peak as seen in Fig 13. There are two parameters in the Lorentzian equation, and one additional parameter in the spike, which can be combined to give  $\beta$  and  $k$ . This technique is applied independently to each of the dimensions in the sample plane  $x$  and  $y$ , except the  $\beta$  calibration which is only applied in

one dimension, as the AOM is only one dimensional. This method was originally developed by Svoboda and Block[7], but the derivation and method outlined here is from [45].

$$\gamma\dot{x}(t) + k[x(t) + A\sin(2\pi f_{drive}t)] = F_{thermal} \quad (6)$$

Eq. (6) is the equation of motion for a spherical bead in a trap undergoing sinusoidal oscillation.  $\gamma$  is the drag coefficient of the bead,  $k$  is the trap stiffness,  $x$  is the bead's position,  $A$  is the amplitude of the laser's oscillation,  $f$  is the driving frequency and  $F$  is the random thermal force driving Brownian motion. The first term on the left represents viscous drag, the second, the force of the trap of the bead, and the right side is the thermal force.

$$P_{thermal}(f) + P_{osc}(f) = \frac{D}{\pi^2(f^2 + f_c^2)} + \frac{\frac{1}{2}f_c^2 A^2}{(f^2 + f_{drive}^2)} \delta(f - f_{drive}) \quad (7)$$

Now by Fourier transforming the general solution to Eq. (6), we can find the one-sided power spectrum of the position data (Eq. (7)), which is divided into two parts: the thermal contribution and the trap oscillation contribution. The thermal contribution is the first term and trap oscillation contribution is the second term.  $D$  is the diffusion coefficient,  $f$  is the independent variable (frequency after the Fourier transform),  $f_c$  is the critical frequency, and  $f_{drive}$  is the oscillation frequency. Fitting the power spectrum of the raw position data with Eq. (7) will extract the parameters  $D$ ,  $f_c$ , and  $A$ , which can be used to obtain  $\gamma$ ,  $k$  and  $\beta$ .  $\beta$  is determined by dividing the known theoretical power in the oscillation peak by the experimentally measured power as in Eq. (8).

$$\beta = \sqrt{\frac{W_{th}}{W_{exp}}} \quad (8)$$

where  $W_{th}$  is the second term in Eq. (7) and  $W_{exp}$  is the experimentally measured power in the oscillation peak. Once we have the parameters  $D$  and  $f_c$  from the fit, then we use Eqs. (9) and (10) to obtain  $\gamma$  and  $k$ .

$$\gamma = (k_B T)/(\beta^2 D), \quad (9)$$

$$k = 2\pi f_c \gamma, \quad (10)$$

where  $k_B$  is Boltzmann's constant and  $T$  is the temperature in kelvin.

### **The FDT Method**

There are three parts to an experiment in our application of the FDT method as seen in figures 14-16 [23, 24]. The  $\beta$  conversion calibration involves trapping the object of interest, and then oscillating the detection laser over it. We oscillate the detection laser, using an AOM, with a triangle wave of known amplitude (typically 40-80nm) and frequency (typically a few thousand Hz), and then divide the known amplitude by the measured voltage amplitude on the QPD. This procedure is done once per data acquisition, at the beginning of the acquisition. The high frequency is required to avoid low frequency noise, cellular processes, and to minimize the amount of time spent on this acquisition.

The passive calibration simply records position data for the cargo in the trap, with no trap or detection laser activity, while the active spectrum records position data for the cargo in the trap while the trapping laser is being actively oscillated. This oscillation is the sum of many sinusoidal oscillations at different frequencies being added together (we typically oscillate at 20 different frequencies from 300 Hz to 16000Hz, with oscillation amplitudes of 10-40 nm). Data acquisition typically occurs for slightly more than 7 seconds, with a short  $\beta$  conversion period, then alternating half second periods of active and passive calibration. The calibration occurs throughout data acquisition, and although the trap is oscillating it has minimal effect on the cargo's position, generally only being visible in the Fourier transform of the position data. This calibration could be applied independently to each dimension  $x$  and  $y$  in the sample plane, but as

the AOMs are one dimensional, is only applied in one, and it is assumed that the local environment and trapping potential are reasonably symmetric in the sample plane.

The theoretical technique for this technique was developed by Fischer and Berg-Sorensen, and was tested by them in *in vitro* F-actin solutions. The theory explained here is a summary of their original theory paper.

The Passive Step

$$m\ddot{x}_U(t) = - \int_0^\infty \gamma_{1,U}(\tau)\dot{x}_U(t-\tau)d\tau - \int_0^\infty \gamma_{2,U}(\tau)\ddot{x}_U(t-\tau)d\tau - kx_U(t) + F_{thermal}(t) \quad (11)$$

Eq. (11) is the Langevin equation of motion for the passive system, with the subscript U indicating the system is undriven. The  $x$  terms are the position of the trapped particle at time  $t$  and its various derivatives,  $m$  is the mass of the trapped particle,  $k$  is the trap stiffness,  $F_{thermal}$  is the thermal force, and the  $\gamma$  terms represent viscoelastic and hydrodynamic memory effects. These terms reduce to the viscous drag in an *in vitro* viscous system, but in a complex viscoelastic environment, it is necessary to take into account viscous and elastic effects. The integrations involving past velocities and accelerations over time are necessary to take into account the changes and inertia of the local environment that lead to history dependent forces, like when the trapped particle moves, the fluid filling its previous position has inertia and therefore exerts a force at a later time on the particle. The term on the left is the inertial term for the trapped particle, the third term of the right is the trapping force, and the last term is the force exerted by random thermal fluctuations, while the first two terms on the left are the viscoelastic terms.

Once again we will take the power spectrum of the passive raw position data which gives us Eq (12):

$$P_U = \frac{2k_B T \text{Re}[\tilde{\gamma}_U(\omega)]}{|k + i\omega\tilde{\gamma}_U(\omega) - \omega^2 m|^2} \quad (12)$$

Here the tilde indicates the Fourier transformed version of the variable,  $k_B$  is the Boltzmann constant,  $T$  is the temperature in kelvin,  $\omega$  is the frequency (the independent variable after the transform) and  $\gamma_U$  stands for the complex friction relaxation spectra ( $\tilde{\gamma}_{1,U} + i\omega \tilde{\gamma}_{2,U} = \tilde{\gamma}_U$ ), where the real part accounts for dissipative (viscous) effects and the imaginary part accounts for elastic effects. In a purely viscous environment it reduces to the drag coefficient of the trapped particle. In the power spectrum calibration method it was assumed inertial effects were negligible and the  $w^2m$  term was left out. Removing this inertial term and the complex part of the friction relaxation spectra reduces this power spectrum to the regular one seen in the power spectrum calibration method.

### The Active Step

In the active step we drive the system by oscillating the laser. It is possible to drive the system by oscillating the stage also, which leads to a slightly different set of equations. The Langevin equation of motion is more or less the same to start, with an added term  $X_L$  for the laser driving. The subscript D stands for the driven system.

$$m\ddot{x}_D(t) = -\int_0^\infty \gamma_{1,D}(\tau)\dot{x}_D(t-\tau)d\tau - \int_0^\infty \gamma_{2,D}(\tau)\ddot{x}_U(t-\tau)d\tau \quad (13)$$

$$-k[x_D(t) - x_L(t)] + F_{therm}(t)$$

The active position data is not treated in quite the same manner as the passive, and a simple Fourier transform of it is taken and used in the next set of equations. The next step is to look at the response function  $\epsilon(\omega)$  of the system, which is defined as:

$$\tilde{x}_{dr}(\omega) = \epsilon(\omega)\tilde{F}_{ext}(\omega) \quad (14)$$

This relates the average motion of the trapped particle to the external force, and the tilde once again indicates a Fourier transform. Trapped objects in viscoelastic media have a response function of:

$$\epsilon(\omega) = 1/[k + i\omega\tilde{\gamma}_D(\omega) - \omega^2m] \quad (15)$$

This can be seen from the early equation for the power spectrum of the undriven system where the bottom portion was the complex conjugate of the response function and the top portion was the thermal force. In order to simplify analysis, we introduce a magnitude called the active spectrum,

$$\tilde{R}_L(\omega) \equiv -\frac{k}{i\omega}\epsilon(\omega) = \tilde{x}_{dr}(\omega)/-i\omega\tilde{x}_L(\omega) \quad (16)$$

This active spectrum is the part we actually use in the analysis, and it simply consists of the Fourier transform of the cargo's position data at frequency  $\omega$  from the detection QPD, divided by the Fourier transform at frequency  $\omega$  of the laser position data from the laser QPD. The  $i$  on the bottom simply indicates that the magnitudes of the two positions also have phases, which can be looked at as angles on the complex plane, and the  $i$  swaps the in and out of phase components.

The next step in the calibration is the combination of the active and passive data, and involves the fundamental assumption behind this calibration, that the Fluctuation-Dissipation Theorem holds. This means that the active and passive data's friction relaxation spectrums ( $\gamma$ ) are the same, that the environment's response to the active calibration's perturbations is linear. Another way to look at it is that the passive environment and the active environment (explored by oscillations of the same size as the Brownian fluctuations during the passive measurement) are the same. This assumption has to be met because in viscoelastic environments, crushing or stretching the environment can cause changes in the local relaxation spectra. This is why it is necessary to keep the active oscillations on the same order of magnitude as passive Brownian motion. If this assumption holds, it leads to:

$$k_\omega = 2k_B T \frac{Re[\tilde{R}_L(\omega)]}{P_U(\omega)}, \quad (17)$$

where  $\text{Re}$  indicates the real component of a complex number,  $P_U$  is the power spectra from Eq. (12), and  $k_\omega$  is the trap stiffness at frequency  $\omega$ , although all  $k_\omega$  should be the same at the time scales in which we are interested. This is the final equation that calibrates the trap's stiffness. To get this out of the trap laser and cargo position data we collect in an experiment, we take the power spectrum of the passive data to get  $P_U$ , we put the laser and cargo position active data into Eq. (16), and then take the real component to get  $\text{Re}[\tilde{R}_L(\omega)]$ , after which we put them into Eq. (17) and get the stiffness. We then average over all the frequencies we oscillated at to arrive at the final stiffness. This entire process might not be entirely clear as to what is happening in all the equations, but a simple way to think of it is as thus: we need to determine four things in our viscoelastic-environment trap calibration. The first,  $\beta$ , is discovered in the first step of the calibration. The last three,  $\text{Re}(\gamma(\omega))$ ,  $\text{Im}(\gamma(\omega))$  and  $k$  we get from the active and passive steps, where  $\text{Re}(\gamma(\omega))$  is the viscosity at  $\omega$ ,  $\text{Im}(\gamma(\omega))$  is the elasticity at  $\omega$ , and  $k$  is the trap stiffness. We have three unknowns and three measurements. The passive amplitude at  $\omega$  (from  $P_U(\omega)$ ), the active amplitude at  $\omega$  (from  $\tilde{R}_L(\omega)$ ) and the phase difference between the laser's oscillation and the particle's oscillation at  $\omega$  (also from  $\tilde{R}_L(\omega)$ ) are the three measurements. These three measurements can essentially be thought of as: an amplitude measurement of the trap and environment damping the particle (passive), an amplitude measurement of the trap versus the environment (active), and a measurement of the phase delay between an externally imposed trap force and the response of the trapped particle to it (active).

## Section 2.4: The Assays

This section will go through the assays: how they are prepared, how they are carried out, and any materials or methods involved in them.

## Live Cell Stall Force Assays

Assays were performed in A549 cells from American Type Culture Collection (ATCC, CCL-185) and *Dictyostelium discoideum* strain Ax-2 #DBS0235518 (Dictybase). A549 cells were grown on glass bottomed petri dishes (WilcoWells) at 37 degrees Celsius, 5% CO<sub>2</sub>, in F-12K (Kaighn's modification of F-12) with 10% Fetal Bovine Serum, penicillin and streptomycin. The assay was carried out at room temperature under standard atmosphere in the same medium. The *Dictyostelium* cells were grown in flasks at 21C in DB (Development Buffer, 5 mM Na<sub>2</sub>HPO<sub>4</sub>, 5 mM KH<sub>2</sub>PO<sub>4</sub>, 1 mM CaCl<sub>2</sub>, 2 mM MgCl<sub>2</sub>, pH 6.5) with E. Coli strain B/r neomycin resistant. Carboxylated latex beads (520 nm diameter, Spherotech) were added to the flask anywhere from 2 hours to the night before the assay. The cells were then placed on a coverslip for at least 30 minutes, a thin sheet of agar was placed upon them to flatten them out, and any excess medium was removed. A microscope slide was then placed on the top of the agar (agar overlay method [47]). A549 cells were observed at room temperature on the optical trap for up to three hours, *Dictyostelium* cells were observed for less than two hours as they generally appeared to become unhealthy when left under the agar overlay for longer periods of time. Lipid vesicles were trapped in the A549 cells, while phagocytosed beads were trapped in the *Dictyostelium* cells.

The actual experiments consist of searching among the cells for vesicles of trappable size (generally around 500 nm or greater in diameter) that were motile and reasonably isolated from other vesicles that could interfere with the measurement. After finding a vesicle that met these criteria, the trap's position was centered on it, first by hand, and then when the program started, was centered again on the vesicle programmatically. This was necessary as in the cell the vesicles are not free to move around as they are *in vitro* and they do not fall to the center of the

trap automatically unless the trap is within the region where the vesicle is free to move (generally within 100 nm or so). If the trapped vesicle is not in the center of the trap, the calibration will be off. This will be picked up in the data analysis later and thrown out, but it still generates a lot of useless data.

After the centering, the trapping laser was turned on and the vesicle was trapped. The detection laser was oscillated for the  $\beta$  calibration, then the passive and active calibrations occurred for a half second each, alternating for seven seconds total. The trap was then shut off, and the data displayed. If the vesicle showed any significant motion that appears to have led to a stall, the data was kept, if not, the data was thrown away. Then the process was repeated. The majority of seven second acquisitions are useless because the vesicle doesn't stall, normally because it doesn't move. The reason data acquisitions were seven seconds long is seven seconds of calibration data is the most that the program and computer being used can hold before they stop working. The experimental data consist of the trapped particle's position recorded on a QPD at 80 kHz, a CCD camera recording of the sample plane imaged with brightfield microscopy at 20 Hz, and a QPD record of the trapping laser's position, also recorded at 80 kHz.

### ***In Vitro* Motor-Coated Bead Assays**

5 *in vitro* bead assays were performed: beads coated with dynein, kinesin, or dynein and kinesin in buffered water, beads in viscoelastic media, and beads coated with kinesin in a viscoelastic media. The kinesin-coated beads were created by incubating 1  $\mu$ L beads with 1  $\mu$ L of diluted kinesin (anywhere from no dilution to 1:10,000 dilution). The kinesin and beads were diluted in BRB-80 (PIPES 80 mM pH 7, 1 mM EGTA, 1 mM MgCl<sub>2</sub>). The mixture was allowed to sit on ice for at least 15 minutes, and then was mixed into an imaging buffer consisting of 80  $\mu$ L BRB-80, 10  $\mu$ L BRB-80 + 20 mg/mL BSA (Bovine Serum Albumin), 4  $\mu$ L 100mM MgATP,

1  $\mu$ L 2.5 M PCA (3,4-Dihydroxybenzoic acid, Fluka #37580), 1  $\mu$ L 50  $\mu$ M PCD (Protocatechuate 3,4-Dioxygenase, Sigma #P8279), 2  $\mu$ L 1M DTT. The PCA/PCD is an oxygen scavenging system (without it the trap creates free radicals that kill the motors quite quickly), the DTT is to keep the system reduced (we generally find *in vitro* motors will not walk at all without a reducing agent), the BSA is to coat the beads and the sample chamber to prevent sticking, and the MgATP is necessary to supply ATP to power the motor, and for the magnesium which is necessary for kinesin's catalytic site to function. PIPES is used as buffer for its pH buffering range and due to the fact that it is widely used in cytoskeletal motor assays, although imidazole, HEPES and other buffers have also been used successfully. Low salt concentration is also necessary, as high salt, in particular sodium, interferes with motor binding to microtubules. After suspending the beads in imaging buffer, they are sonicated briefly in a chilled bath sonicator to break up clumps. Clumping occurred sporadically, with some samples not needing sonication at all, while others would require up to 5 minutes of sonication to reduce clumping.

Beads with dynein have a slightly different binding protocol. BRB-80 was replaced in all solutions with Dynein Motility Buffer (DMB) with 8mg/mL BSA added. DMB consists of 30mM HEPES pH 7.2, 50mM KAcetate, 2mM MgAcetate, and 1mM EGTA. The dynein was generally diluted from 1:1 to 1:10, as it showed much less motility than kinesin at similar concentrations. The dynein, or dynein and kinesin were incubated with the beads for a minimum of thirty minutes. In experiments with kinesin and dynein coated beads, the directionality of the axonemes was determined by adding kinesin-only beads of a different size to the imaging buffer, and determining kinesin's direction of travel on every axoneme used to take data.

The bead assays in viscoelastic media were carried out in the same solutions as the normal kinesin-coated bead assay, except that hyaluronan (HA: Lifecore Biomedical, HA20K-1,

HA100k-1, HA-200K-1) was added to the imaging buffer at various concentrations (0 mg/mL, 1, 2 ...10 mg/mL). Hyaluronan is a polymer of glycosaminoglycan, a principle component of the extracellular matrix that can create a viscoelastic environment at sufficient concentrations. The sample chambers had to be constructed in a slightly different manner, as the HA thickened the imaging buffer to the extent that it would not perfuse through a chamber. The slide used for the chamber had two holes drilled in it with diamond coated drill bits and after the coverslip was sandwiched on top of the slide with double-sided sticky tape, epoxy was used to seal the open sides of the chamber. The solutions were then introduced through the drilled holes and pressure from the micropipette pushed the solutions through the chamber.

The sample chambers for the rest of the *in vitro* experiments were prepared as follows: 2 pieces of double sided sticky tape were applied to a glass slide leaving a gap between them and a glass coverslip (#1.5 thickness was used due to imaging requirements of the objective) was sandwiched on top, leaving a sample chamber approximately 20  $\mu$ L in volume, into which solutions were flowed by perfusion, using a Kimwipe to provide pull. Axonemes were diluted 1:20 in BRB-80 and flowed into the chamber, then the chamber was placed coverslip side down in a refrigerator for 15 minutes minimum to allow the axonemes to stick to the coverslip surface (cold helps the axonemes stick). Then BRB-80 with 20 mg/mL BSA was flowed into the chamber and allowed to sit for 10 minutes to block the surface of the chamber after which the chamber was ready for the sample.

### **Organelle Purification and Stall Force Assays**

*Dictyostelium* cells were grown until most of the E.coli was eaten, immediately before the *Dictyostelium* started to aggregate. 500 nm beads (Spherotech) were then added to the flasks from 1 hour to 12 hours before purification. The following purification protocol is modified

from [35, 39]. Cells were collected, centrifuged and resuspended in ice-cold Sorensen's buffer (8g  $\text{KH}_2\text{PO}_4$ , 1.16g  $\text{Na}_2\text{HPO}_4$  into 4L, pH 6.0). Centrifugation was typically at 100g for 3 minutes, and repeated 3 times, just enough to pellet the *Dictyostelium*, but not free beads or *E. coli*. After the final centrifugation, the pellet was resuspended 1:2 in Lysis Buffer + protease inhibitors + 30% sucrose w/v (LB30%+PI), which is: 30 mM Tris-HCl (pH 8), 4 mM EGTA, 3mM DTT, 5 mM benzamidine (Sigma 434760), 10  $\mu\text{g}/\text{mL}$  soybean trypsin inhibitor (Sigma T6522), 5  $\mu\text{g}/\text{mL}$  TPCK/TAME (Sigma T4626, T4376), 10  $\mu\text{g}/\text{mL}$  leupeptin, pepstatin A and chymostatin (Sigma L2884, P5318, C7268), and 5 mM PMSF. The protease inhibitors were made as follows: benzamidine, made fresh every time and suspended in LB at 200mM; soybean trypsin inhibitor at 4mg/mL and 5 mg/mL TAME in ddH<sub>2</sub>O, aliquoted, flash frozen and stored at -20C; chymostatin, leupeptin, pepstatin A, and TPCK each at 10 mg/mL in DMSO, aliquoted, flash frozen and stored at -20C; PMSF 400 mM in isopropanol, stored at -20C, must be heated to 37C and shaken to resuspend, made fresh monthly due to degradation in water. After resuspension the cells were lysed by passage through a 5  $\mu\text{m}$  polycarbonate syringe filter, centrifuged at 20000g for 20 minutes, and the supernatant was collected. The supernatant can be aliquoted, flash frozen and stored at -80C for a week, but motility will go down over time. Diluting the aliquots will also reduce motility, as will further purification steps, such as sucrose step gradient centrifugation. More purification typically leads to the loss of negative end (dynein) motility. However, as the phagocytosed beads are a different density than the rest of the cellular debris, it is possible to isolate the phagosomes from other organelles by centrifuging at 20000g for 30 minutes using a 40%, 30%, 10% in LB sucrose step gradient, although dynein motility will be lost. The phagosomes will typically form a white layer at the 30%/10% boundary. Slightly different PI concentrations, different lysing methods, and over purification

all lead to reduced or no motility, so it is recommended to follow the protocol as closely as possible.

The stall force assay for these organelles is very similar to the *in vitro* bead assay except that the BRB-80 is replaced by LB15%+PI. This is necessary as removal of the protease inhibitors stops all motility. Kinesin-coated beads different in size from the organelles (typically 1.2  $\mu\text{m}$  beads from Spherotech) are used to determine the directionality of the axonemes. Care must be taken to ensure debris does not interfere with the trap, as the purified organelles cannot be diluted more than 1:10 without loss of motility and there are large amounts of cellular debris still present in the post-nuclear supernatant.

## **Section 2.5: Data Analysis**

Most data analysis was carried out in Matlab 8.0 with custom made programs. These programs can be found in appendix 1. *In vitro* calibration was carried out by power spectrum fitting in Labview, while *in vivo* calibration and viscoelasticity measurement was carried out post-acquisition in Matlab using the FDT method.  $\beta$  calibration occurs in Labview for both techniques.

Stalls *in vitro* were required to pause for a half second after a displacement of greater than 20 nm from the trap center, and then had to fall back to the trap center. Stall events were selected by eye, after which a program calculated the stall force. *In vivo* stalls were determined with different criteria: greater than a quarter of a second pause before and after the stall and greater than 20 nm displacement. The 20 nm displacement requirement is to ensure a movement larger than the noise background and 20 nm typically corresponds to around 1 pN of trap force. A half second pause is required *in vitro* to ensure stochastic pauses aren't included in stalls, while the fallback indicates the motors haven't simply stuck to the axoneme. The *in vivo*

requirements were chosen due to the special characteristics of the cellular environment. No fallback was required as in the cellular environment fallbacks almost never occurred, mainly due to the fact that the cellular environment appears to be so crowded as to not allow fallbacks. The quarter of a second pause before and after the movement was required to ensure that the vesicle was actually centered in the trap or at least stalled before, and to ensure that stochastic pauses in motility didn't get included as stalls. The *in vivo* stalls were then graded on directionality. Directionality was determined as anterograde (toward the cell membrane, which would typically also be the plus-end of the microtubule) or retrograde (toward the cell center or nucleus, which should typically be towards the minus-end of the microtubule), by observing the ccd camera video of the cell when the stall was measured. Stalls where directionality could not be determined were discarded.

## Section 2.6: Figures

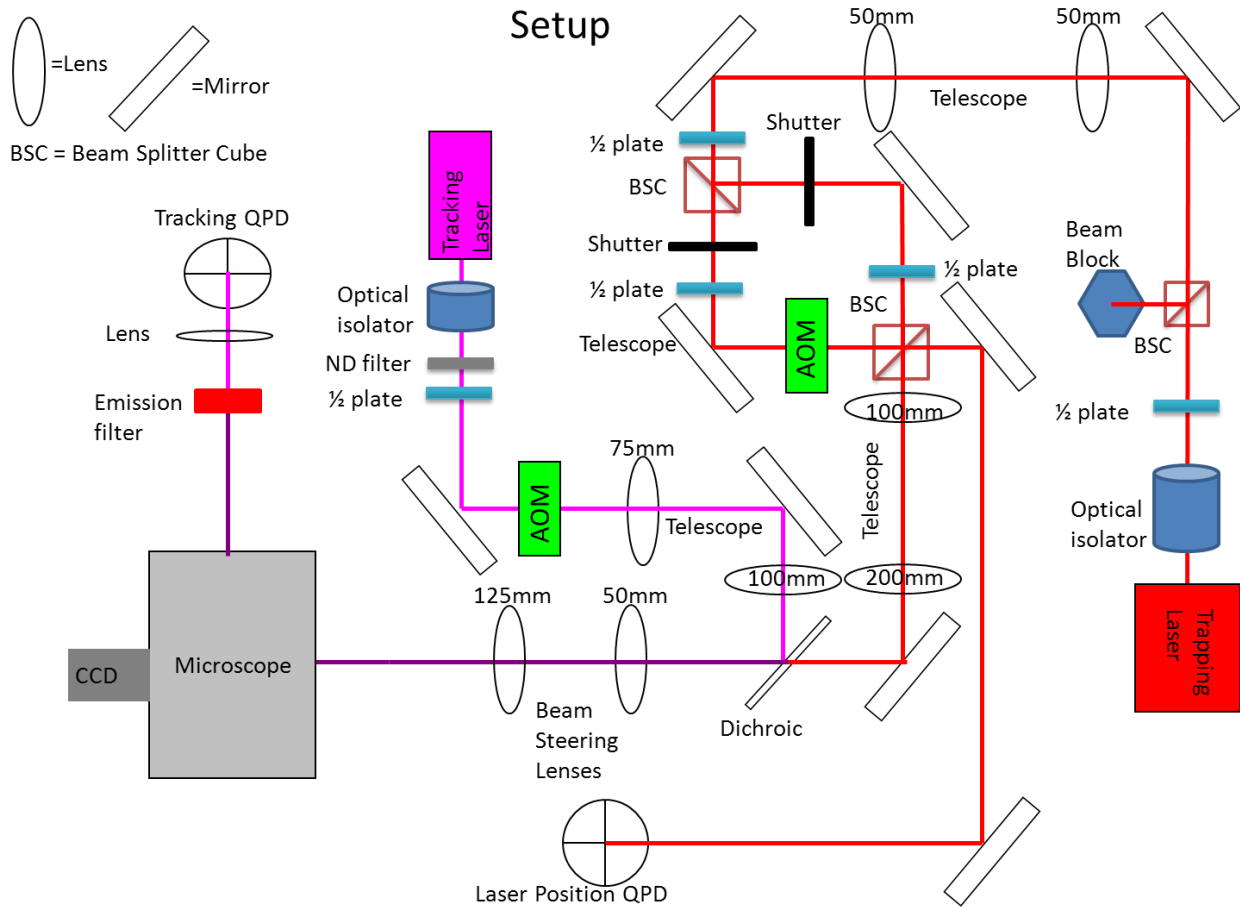


Figure 11: Optical Trap Setup Diagram. This diagram maps out the optical setup of the optical trap used in this experiment. The numbers in or next to the lenses indicate focal length,  $\frac{1}{2}$  plate is a half-wave plate to control the laser's polarization, AOM is Acousto-Optic Modulator, telescope stands for a lens telescope of 2 lenses to magnify and collimate the beam, and ND filter is Neutral Density filter, to weaken the laser.

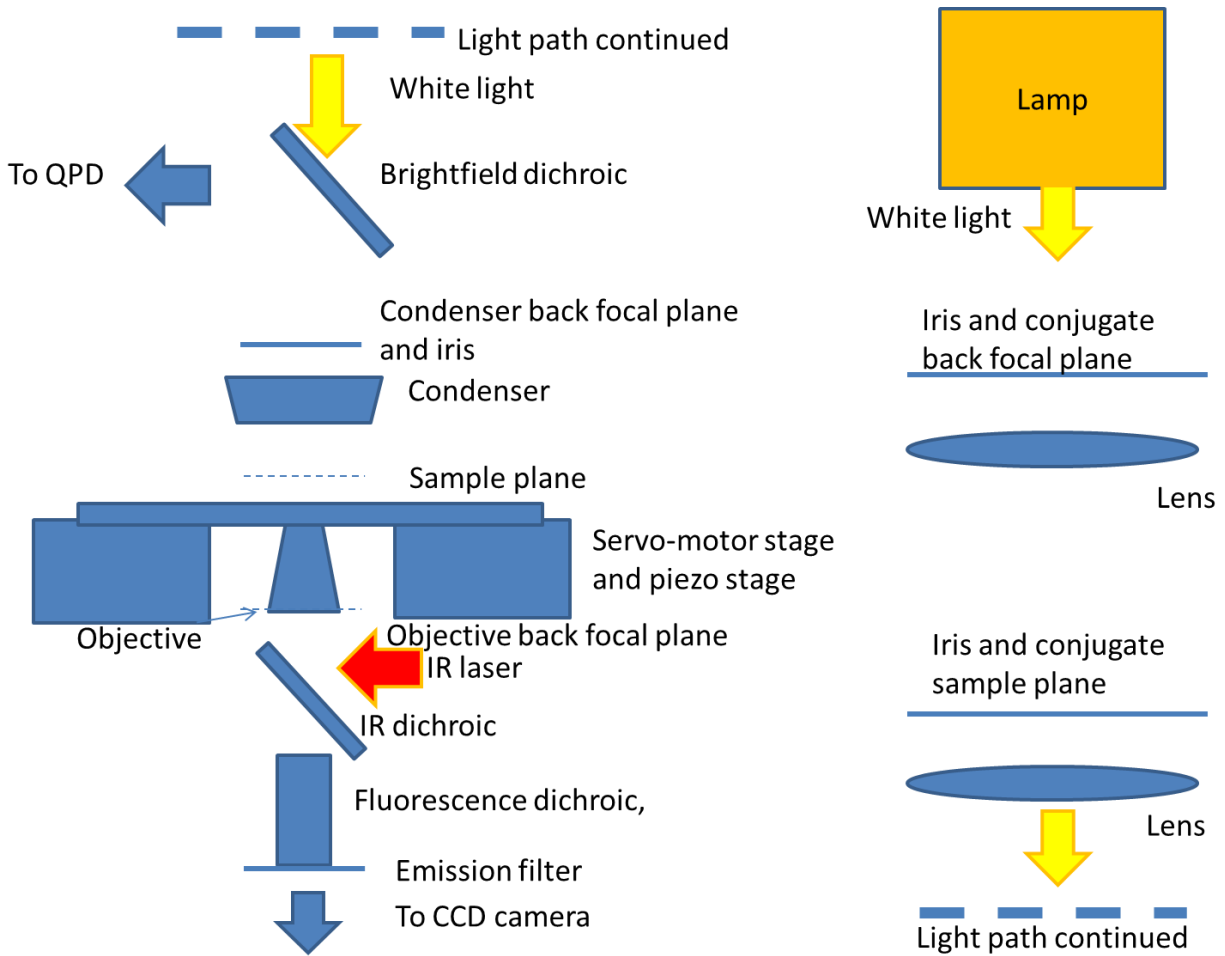


Figure 12: Optical Trap Microscope Light Path. A diagram of the trapping and detection laser and brightfield light path in the microscope. The right side of the diagram shows the extra optics added to map an iris onto the condenser back focal plane. The iris at the conjugate bfp was mapped onto the actual bfp of the condenser in order to allow us to keep the condenser iris open to collect more detection laser light. The bfp condenser iris provides contrast for brightfield imaging however, so without it images of the sample plane could not be taken with any clarity. By using the conjugate iris we could collect all the laser light and still obtain contrast enough to image with the ccd.

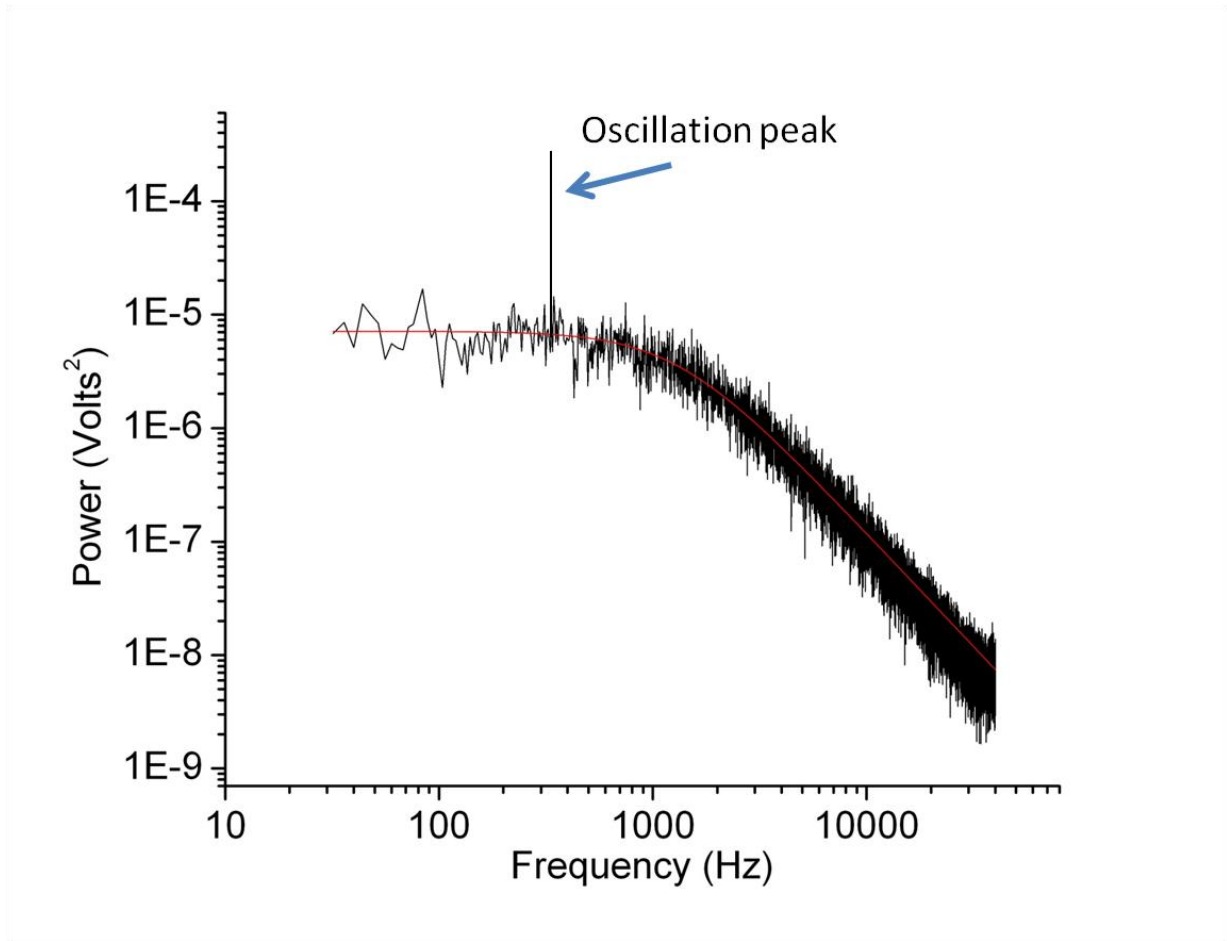


Figure 13: Power Spectrum Calibration. This shows a typical power spectrum graph for trap calibration. The black line is the raw data, the red line is the fit. The oscillation peak, which is used to calibrate  $\beta$ , is cut out for the fit.

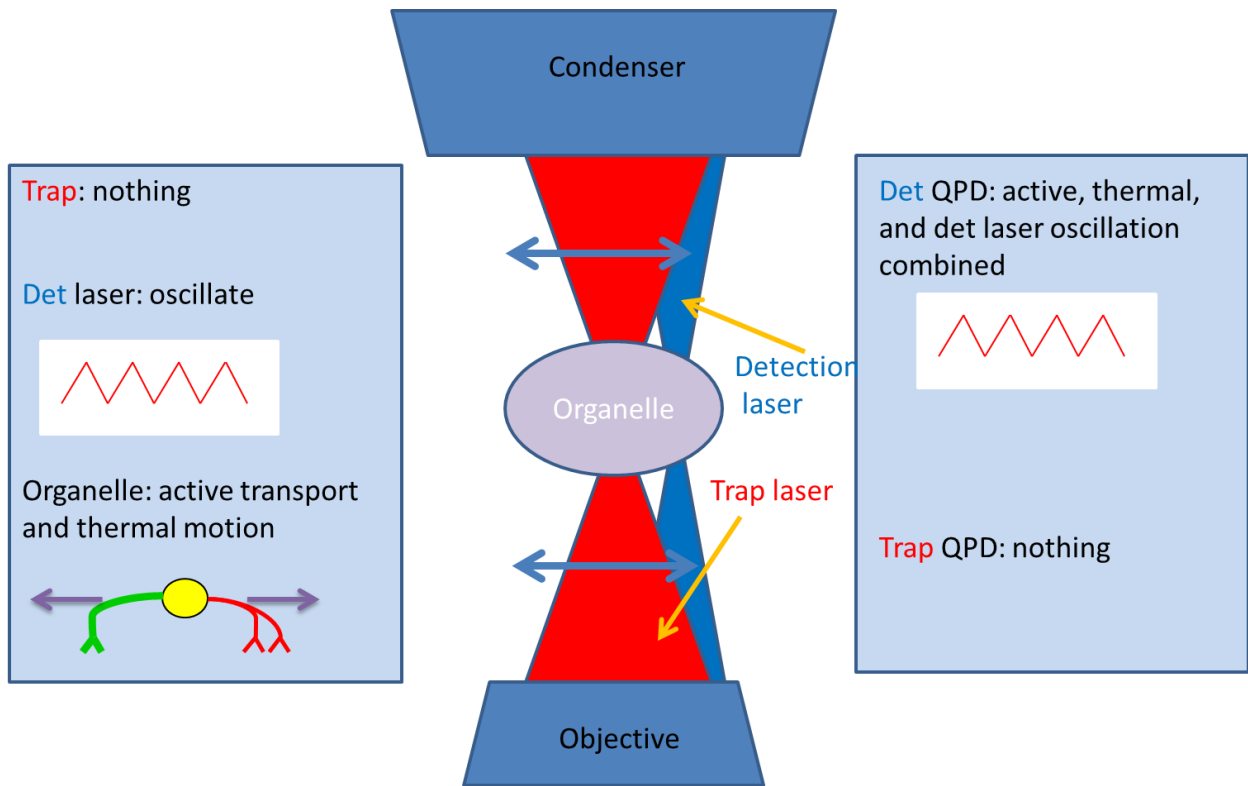


Figure 14: Detection Laser ( $\beta$ ) Calibration. This is an illustration of what is going on during the  $\beta$  calibration in the FDT method. The left hand side is the inputs, nothing from the trap, a triangle wave from the detection laser, and cellular motion. The center shows what is happening at the sample plane. The right hand side shows what the QPDs' read out, in this case a triangle oscillation on the detection laser QPD with some noise from cellular processes.

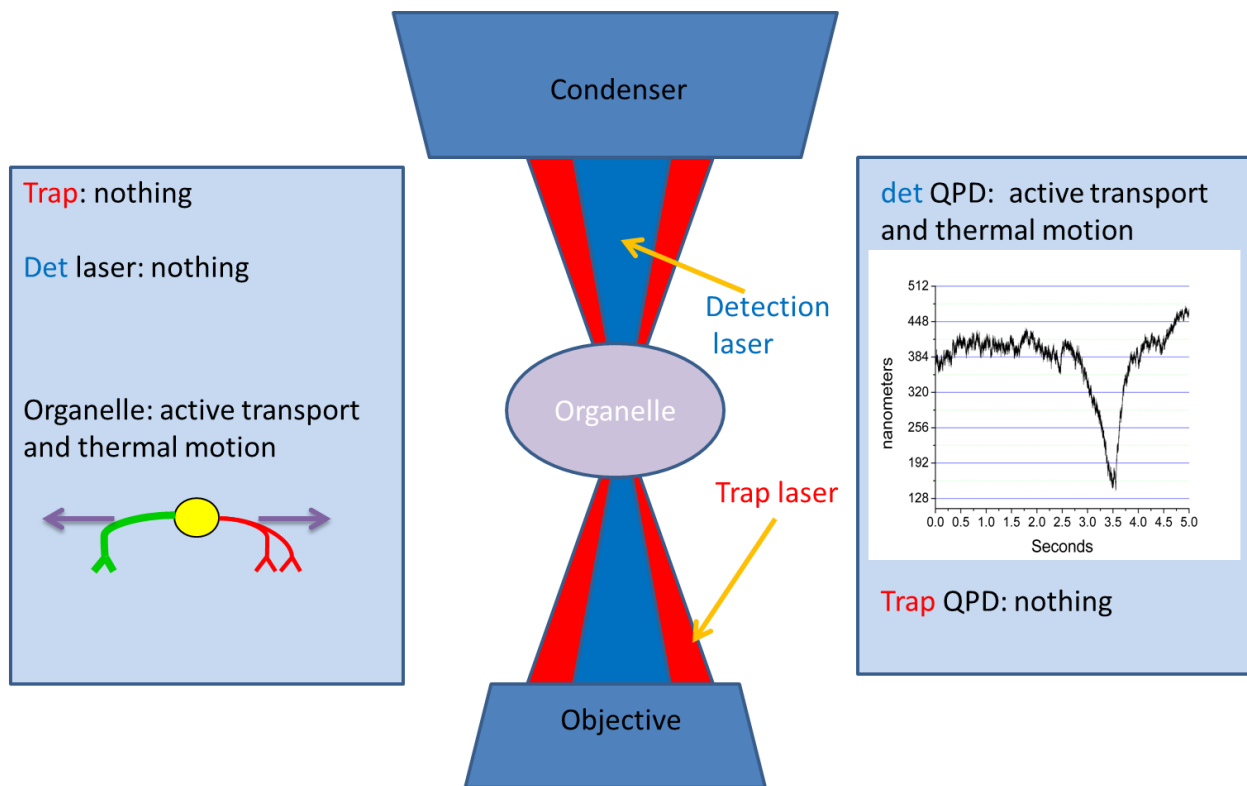


Figure 15: Passive Calibration. An illustration of what is occurring during the passive calibration step. The inputs on the left hand side are solely from cellular activity. The sample plane has nothing occurring except for organelle motility, and the right hand side shows active transport and noise on the detection QPD.

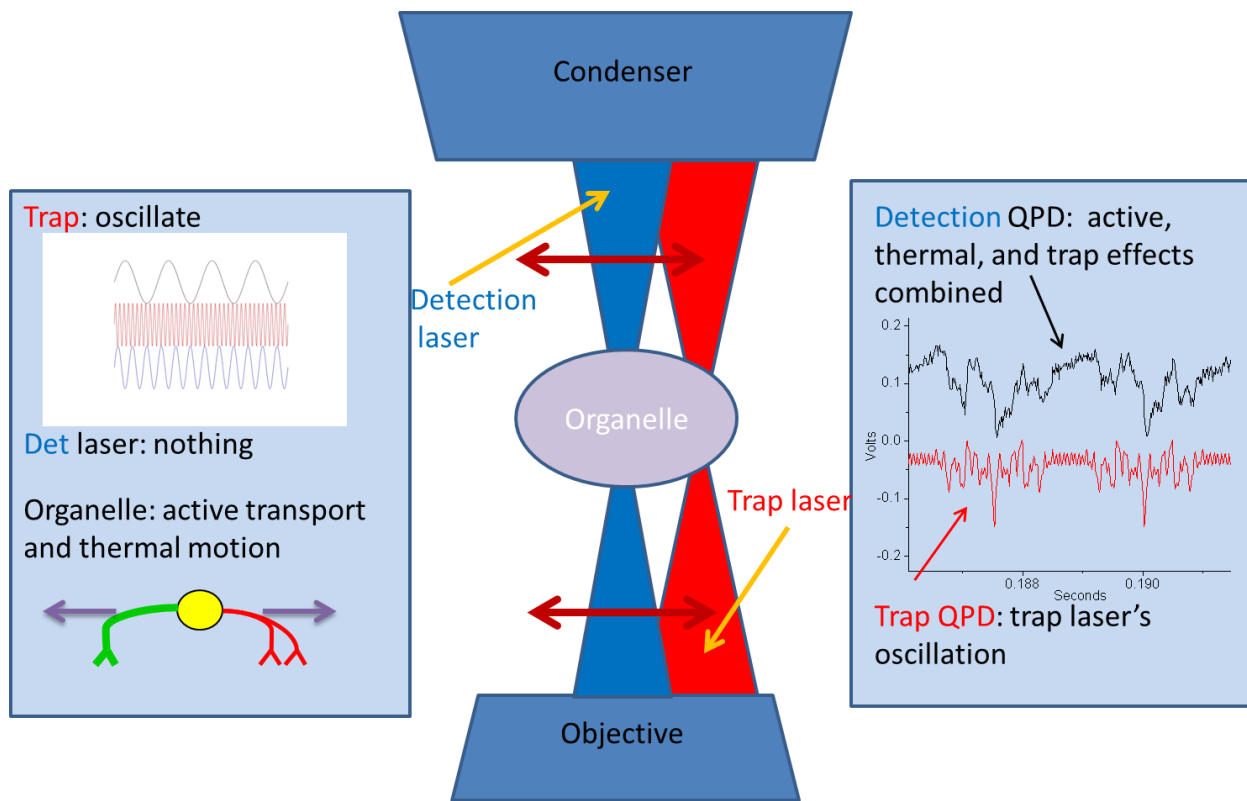


Figure 16: Active Calibration. An illustration of what is occurring during the active calibration step of the FDT method. On the left hand side, the trap is oscillating at multiple sinusoidal frequencies, and the organelle is moving around. The center shows the sample plane where the trap laser is oscillating, and the organelle is moving. The left hand side shows the read out, where the detection QPD is reading out the organelle motion combined with the oscillation imposed by the trap movement, and the trap QPD is reading out the trap laser's oscillations. The graph shown representing the QPD read outs is actually taken from an experiment in water in order to emphasize the oscillation in the detection laser channel. In a cell, the oscillation in the detection laser channel would not be apparent until a Fourier transform is performed.

## Chapter 3: Results

Several experiments will be discussed in this section. The end result of these experiments is the measurement of stall force and motor copy number *in vivo*. The first set of experiments is *in vitro* controls to determine if the homebuilt trap and trap calibration method work appropriately. These experiments include measuring the stall force of kinesin-1 attached to a bead in viscous and viscoelastic conditions, and measuring the viscoelasticity of polymer gels of various densities. The last set of experiments involve measuring stall forces of organelles *in vivo*, measuring the stall forces of beads with both kinesin and dynein attached *in vitro* and measuring stall forces of organelles purified from cells.

### Section 3.1: Measurements on Beads *in Vitro*

Measurements on uncoated and kinesin-coated beads in hyaluronan were taken to test the FDT calibration method. The FDT method, in addition to measuring trap stiffness, measures the local viscoelasticity. Measurements of the local viscoelasticity around beads suspended in different concentrations of hyaluronan were in general agreement with measurements made previously using other methods (figure 17) [48]. Viscoelastic materials are typically heterogeneous and this was seen in the hyaluronic acid measurements, but averaged together they are in agreement with the averages of previous measurements. Stall force measurements at different viscoelasticities were taken to determine if the cellular environment's viscoelasticity has any effect on cytoskeletal motors' stall forces (figure 18). The measurements reveal minimal effect from viscoelasticity on the stall force of kinesin, giving average stall forces of 5-7 pN at all viscoelasticities, but there are significant effects on the number of beads that show motility at different concentrations, with significantly fewer beads walking at higher viscoelasticities. This

is presumably due to lower rates of diffusion for the beads and motors attached to them, thereby decreasing the likelihood of binding events. Although all beads used had the same concentration of kinesin bound to them, a concentration low enough that almost no stall force events with more than one motor occurred in water, it is possible that the increasing elasticity and viscosity biased the stall force measurements towards beads with more motors, biasing histograms with higher concentrations of hyaluronan towards higher stall forces. One final issue is that viscoelasticity measurements *in vivo* reveal viscosities and elasticities an order of magnitude higher than we could achieve in our HA assays. Increasing the concentration of HA stopped all motility, and made it extremely difficult to even move the beads around in solution with the trap. This isn't too surprising, as organelles in the cell cannot generally be freely moved around with the trap, but it does leave uncertainty as to whether or not higher viscosity and elasticity would have an effect on motor stall forces.

Stall force measurements on polystyrene beads simultaneously coated with kinesin and dynein were also carried out to provide an *in vitro* reference for our *in vivo* measurements (figure 19). In the minus-end direction there is a large peak at 1-1.5 pN and secondary peaks at 2 and 3 pN, and in the plus-end direction there is a large, spread-out peak at 4-5 pN with a smaller peak at 1-2 pN. These measurements are quite different than stall force measurements on beads coated with only dynein or only kinesin. Stall force measurements on dynein-coated beads alone yielded a histogram with a large peak around 1.4 pN and peaks decreasing in size at around 2-2.5 pN and 3-4 pN. These secondary peaks are due to multiple dyneins binding to the axoneme and contributing to the stall force in an additive manner. The kinesin-only histogram shows a substantial peak between 5-6 pN. The kinesin-only beads in HA also had similar stall force histograms, with clear peaks in the 5-7 pN range, and few counts at forces less than that. The

kinesin and dynein-coated beads' minus-end directed peak is very similar to the dynein alone peak as would be expected, while the plus-end directed peak is not, but both peaks are similar to their equivalent *in vivo* peaks.

### **Stall Force Measurement in A549 cells**

We first sought to measure the stall force of lipid vesicles in A549 cells to compare to previous A549 stall measurements carried out with an *in vitro* stiffness calibration. Lipid vesicle stalls were defined as a pause greater than a quarter of a second before and after a movement greater than 20 nm, and directionality was defined as anterograde (inward toward the cell nucleus) or retrograde (outward toward the cell membrane). Movements with unclear directionality were left undefined and not included in the stall force histograms. Our results can be seen in figure 20, and were significantly different than those previously measured in A549 cells, as we rarely saw stall forces more than 6 pN, and when the stalls were separated into anterograde and retrograde stalls, there was a clear 2-3 pN peak in the retrograde direction, with what appear to be peaks at 2-3 and 4-5 pN in the anterograde direction[22]. This is significantly lower than the previous measurements in both the anterograde and retrograde directions, where the measured averages were 8 pN for anterograde and 7 pN for retrograde, and peaks were seen at 3 and 6 pN in the anterograde, and 4 and 9 pN in the retrograde.

### **Stall Force Measurement in *Dictyostelium* Cells**

We also measured the stall forces of phagosomes in *Dictyostelium* cells in order to compare to the forces measured previously for endosomes purified from *Dictyostelium* [39]. These stall measurements are similar to the A549 measurements in that there is a large 2 pN peak in the retrograde direction, with a more spread out peak from 2-6 pN in the anterograde direction (figure 20). Although it is not clear, it is possible that the spread out 2-6 pN peak is the

combination of 2 peaks similar to those in the A549 measurements. The *in vitro* measurements previously taken on endosomes purified from *Dictyostelium* didn't have clear stall force histograms, and so cannot be directly compared, but the majority of stalls (76%) were around 5.5 pN in the plus-end direction and the rest escaped the trap, while a majority (54%) of minus-end directed organelles stalled between 4-6 pN of force and the rest escaped. However when Soppina et al purified the motors from *Dictyostelium* and attached them to beads they measured stall forces of 1.1 pN for individual dynein and 5.5 pN for individual DdUnc104 kinesin (the type of kinesin found on endosomes in *Dictyostelium* cells) [39].

### **Stall Force Measurement on Purified Phagosomes from *Dictyostelium***

After obtaining the *in vivo* stall force measurements from A549 and *Dictyostelium* cells, attempts were made to purify the organelles we had trapped *in vivo* in order to compare *in vivo* and *in vitro* behavior for the same organelles and motors, as it was a concern that the *in vitro* motors we had been using were not exactly the same as the *in vivo* motors. As different motors can have different stall forces, this would cast doubt on whether the differences measured in the two environments were due to the different environments, or if they were due to differences inherent to the motors.

We have purified and shown organelles from both cell types walk *in vitro*, but the simple purification that leads to bidirectional *in vitro* motion also leaves a large amount of other cellular debris and components floating around that interfere with the trapping assay. Upon further purification, through a sucrose gradient for the phagosomes, minus-end directed motion is lost. However, we were still able to obtain a measurement for the stall force of the plus-end directed motor on the phagosomes, DdUnc-104, with the result giving a 6 pN peak, as can be seen in

figure 21. This result is in agreement with the stall force measurement obtained previously by Soppina et al. of 5.5 pN for the plus-end directed motor on *Dictyostelium* endosomes.

## Section 3.2: Figures

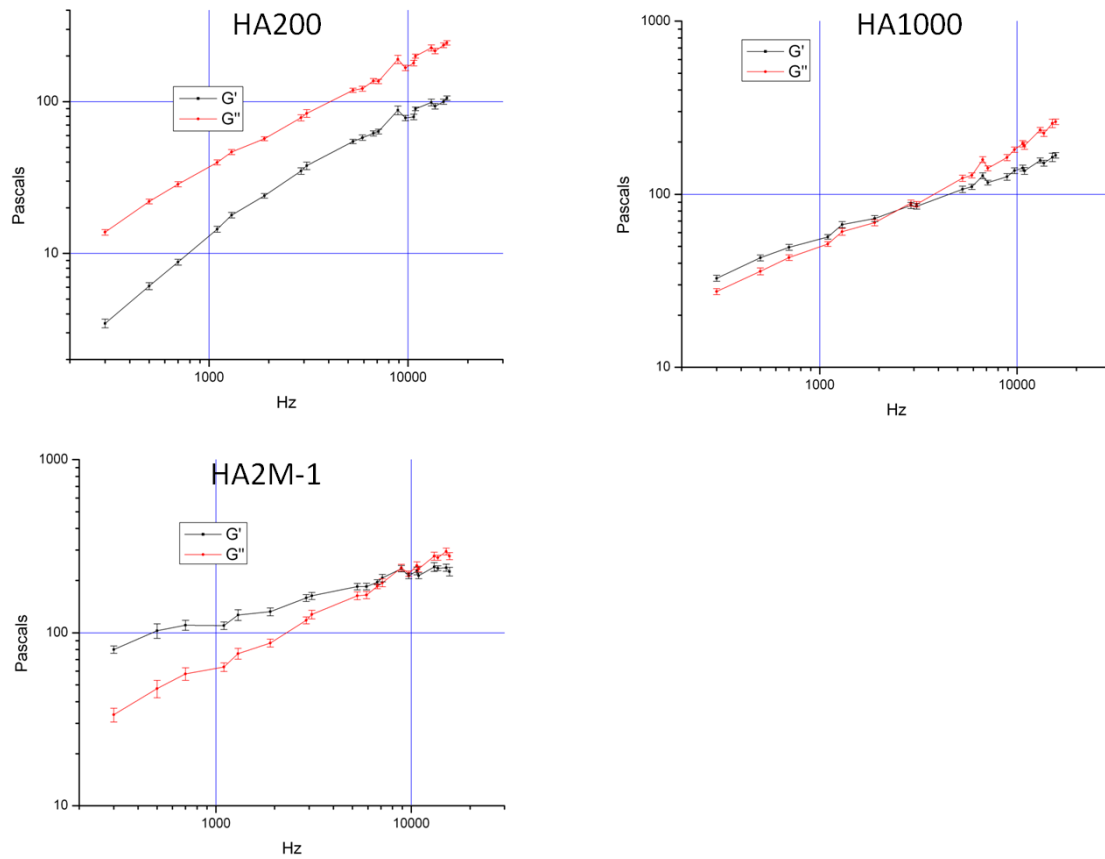


Figure 17: Viscoelasticity Measurements in Hyaluronan. These three graphs show the storage and loss moduli for 10 mg/mL HA solutions, with 3 different polymer lengths: 200 kDa, 1000 kDa, and 2000 kDa. The storage and loss moduli are related to the viscosity and elasticity by  $V=G''/\omega$  and  $E=G'/\omega$  where  $\omega$  is the angular frequency of the measurement. These measurements agree with previous microrheology measurements on HA.

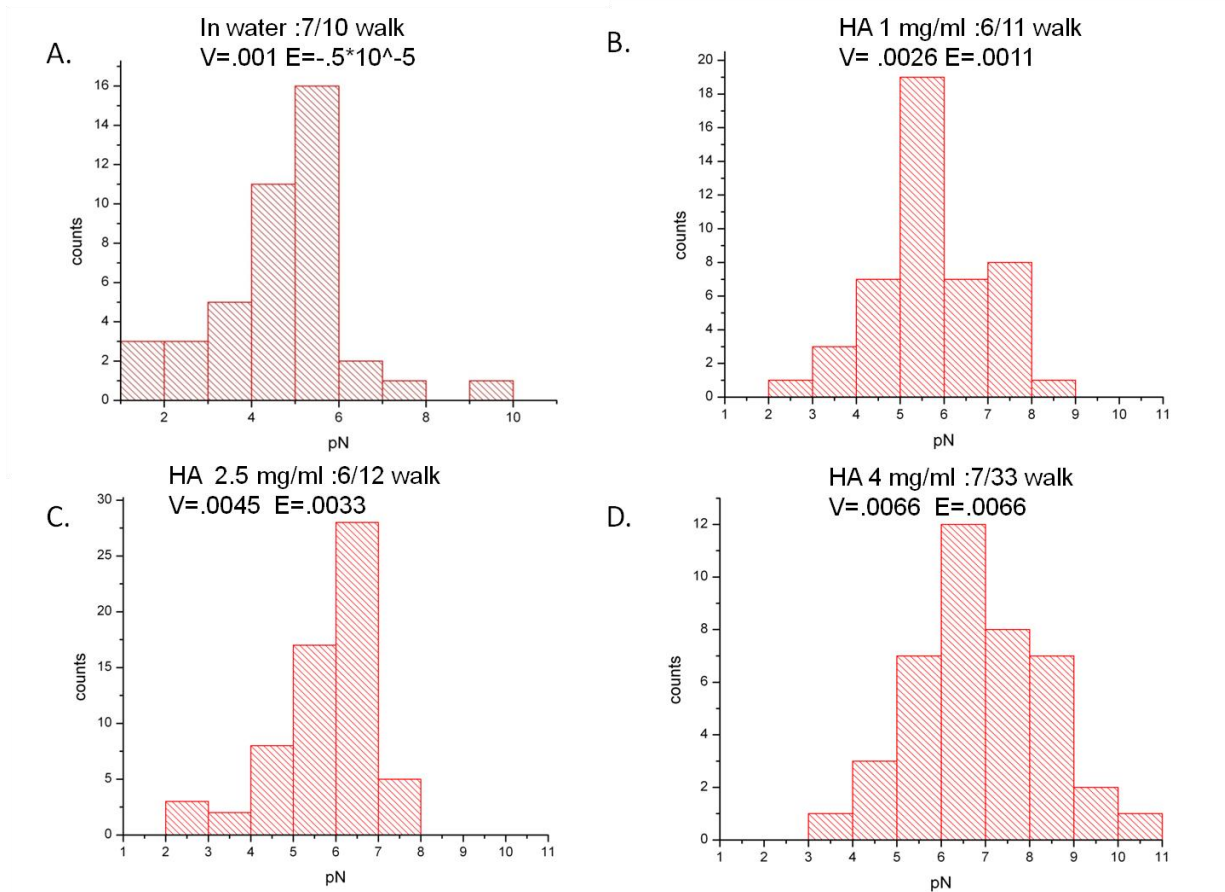


Figure 18: Kinesin-1's Stall Force in HA. These histograms show the response of kinesin's stall force to varying environmental viscoelasticities. V and E stand for viscosity and elasticity and are measured in Pascal\*secs. HA mg/mL is the concentration of HA, and the #/# walked is how many beads walked when brought near an axoneme out of the total tried. Histogram for 5mg/mL HA is not shown as 0/20 beads walked.

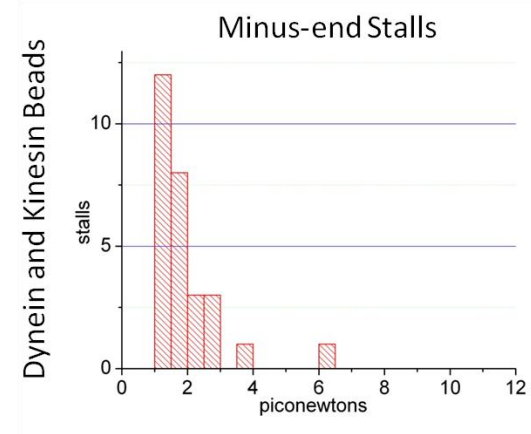
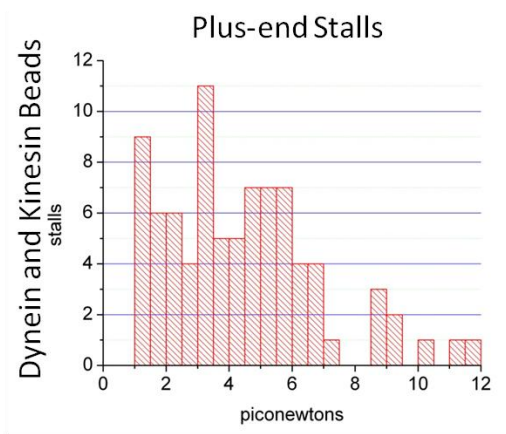
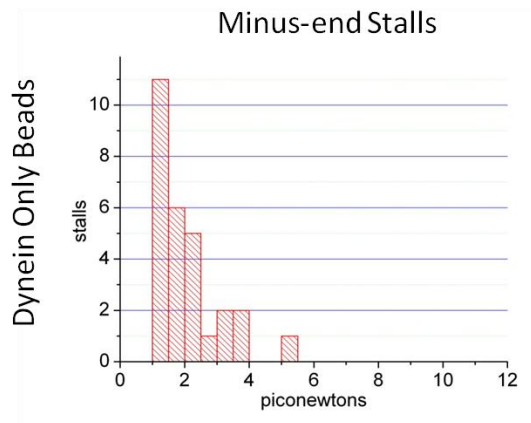
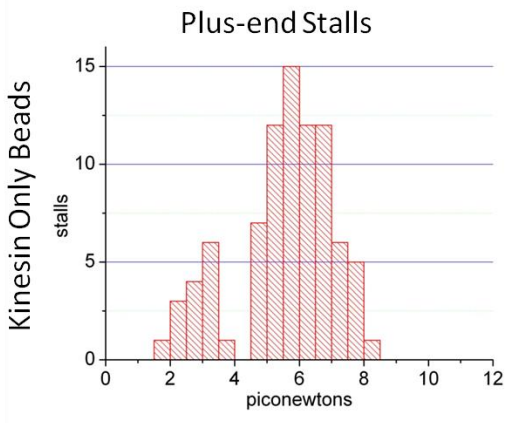


Figure 19: Stall Force of Beads Coated with One Motor Versus Two Motors. These histograms are *in vitro* stall force histograms of beads coated with kinesin, dynein, or kinesin and dynein. There is a significant difference in the plus-end directed histograms between the kinesin-only beads and the kinesin and dynein beads.

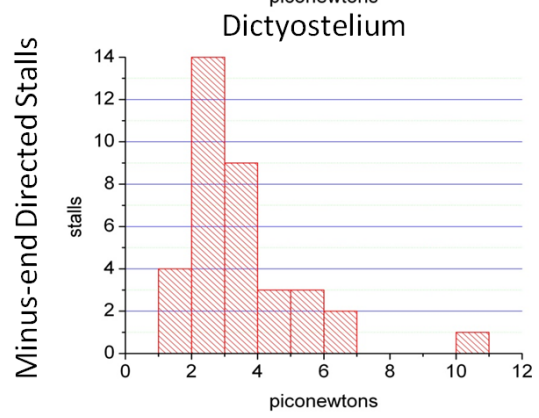
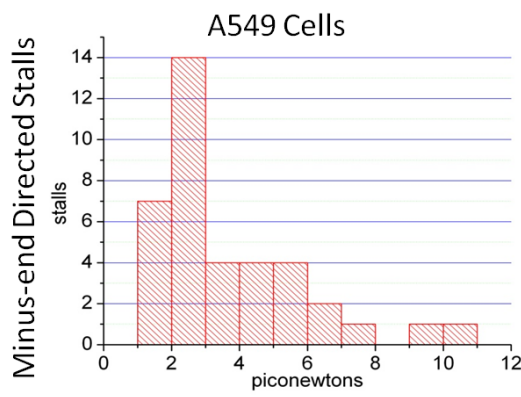
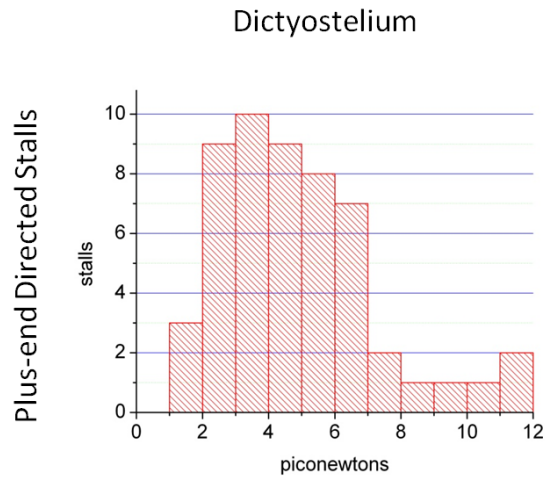
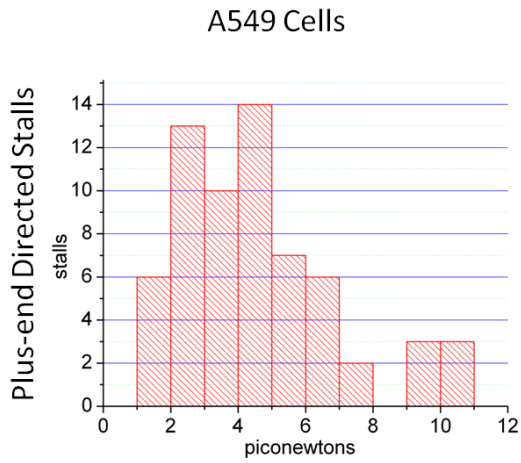


Figure 20: *In Vivo* Stall Force Histograms. This figure shows the stall force histograms from A549 cells and *Dictyostelium*.

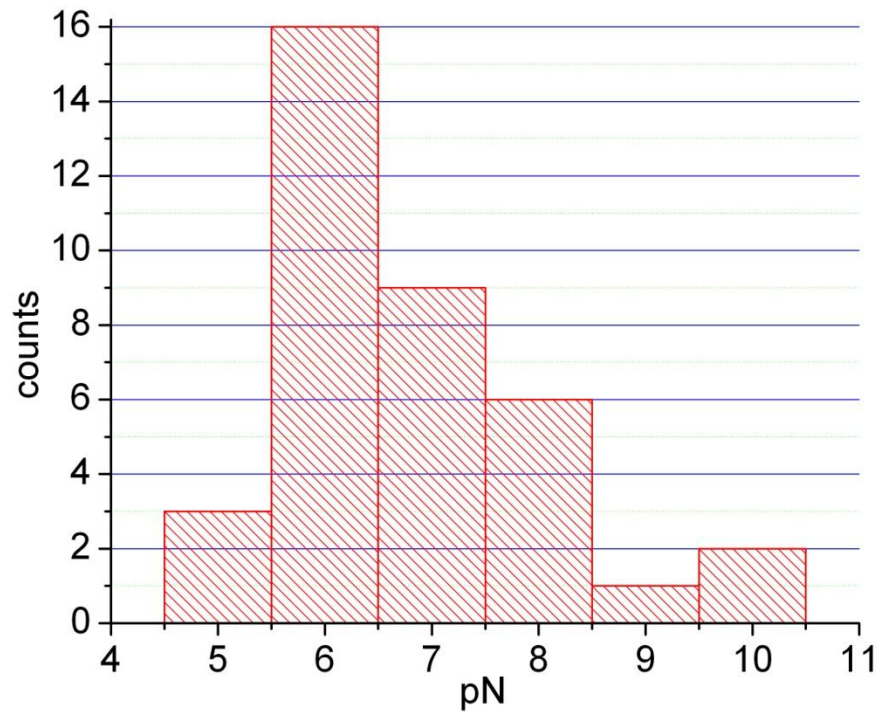


Figure 21: Plus-end Directed Stall Force of Purified *Dictyostelium* Phagosomes. This is the stall force histogram of purified *Dictyostelium* phagosomes that have been purified in such a way as to only reconstitute plus-end directed motion. The motor responsible for plus-end directed motion is DdUnc-104.

## Chapter 4: Discussion

In this section we will discuss the implications our results have for dynein and kinesin's stall forces, motor-environment interactions *in vivo*, motor-motor interactions *in vivo* and *in vitro*, and intracellular transport models such as tug-of-war or coordinated motion.

### Section 4.1: Dynein

Our results support an *in vivo* stall force of 1-3 pN for cytoplasmic dynein and an *in vitro* stall force of 1-2 pN. Our *in vitro* measurements on mammalian dynein-coated beads (stall force of 1.4 pN) agree quite closely with previous *in vitro* measurements, including dynein purified from *Dictyostelium* endosomes and attached to beads *in vitro* (1.1 pN) [39]. There are many possible reasons for the different stalls other groups have measured, from using significantly different types of dynein (such as yeast [9]) to using forms of dynein which are prepared differently [49]. The differences in these measurements has led to the suggestion that most, if not all, *in vitro* dynein constructs are deficient in some way, and that they would have a stall force that is similar to kinesin's if all necessary factors were present.

Our *in vivo* stall force measurements seen in figure 22 reveal an increased stall force for dynein *in vivo* and agree quite well with Shubeita et al's measurement of 2.4 pN and are remarkably close to Ashkin et al's original *in vivo* stall force measurement of 2.6 pN in 1990 [21, 38]. As to why dynein's stall force is larger *in vivo* than *in vitro*, there are several possibilities. The first is that there are necessary factors missing *in vitro* that are present *in vivo* which modulate dynein's stall force. The second is that the dynein being examined *in vitro* is not the exact same type being examined *in vivo*, both are cytoplasmic dynein, but from different organisms. This is true in the case of case of comparing yeast dynein's stall force to mammalian

dynein, but *Dictyostelium* dynein has been purified and its stall force measured as 1.1 pN [39], in agreement with our *in vitro* measurements, while our *in vivo* *Dictyostelium* measurement gave a 2.5 pN stall force. The final possibility is that a 1 pN difference involving *in vivo* measurements, which are noisy, is quite small and is therefore questionable. This would be of more concern if our *in vivo* results hadn't been replicated by two other papers in two different organisms, and the one paper that disagrees with our measurement in A549 cells, disagrees by giving an even higher *in vivo* dynein stall force. However, it is possible that *in vivo* organelles all have a very large number of dyneins attached, leading to at least two dyneins always being active when retrograde motion is occurring. That would lead to a stall force histogram similar to ours, but as dynein attachment should be stochastic, we would still expect to see higher or lower peaks for different numbers of dynein, which we do not. However, as can be seen in figure 22, the *in vitro* dynein-on-beads stall force histogram was taken with a large overabundance of dynein, and this did lead to an increase of the main stall force peak from around 1 pN, to approximately 1.7 pN, so it is possible that a large number of active dynein would appear as a larger stall force.

## **Section 4.2: Kinesin**

With kinesin the differences between *in vivo* and *in vitro* measurements are even more disparate as can be seen in figure 23. Our *in vivo* stalls have peaks at 2 and 4 pN or one large peak spread from 2-6 pN, while the *in vitro* kinesin stall force is 5-7 pN, and is 5.5-6 pN for kinesin purified from *Dictyostelium* by both our measurements and Soppina et al's. The reason for this difference is currently unclear. Ashkin et al, measured 2.6 as the stall force for a single motor in any direction, once again similar to our lab's and Shubeita et al's measurements. Sims et al saw somewhat similar behavior in A549 cells, seeing anterograde stall force peaks of 3 and

6 pN, with the 6 pN peak being quite a bit larger than the 3 pN. Shubeita et al also get a very similar kinesin stall force histogram in *Drosophila* embryos, and postulate that the kinesin they are looking at has a stall force of 2.6 pN, and that the second peak is simply 2 kinesins working together[18, 21, 22, 39]. The fact that we and other groups have measured the *in vitro* stall force of a kinesin (6 pN) from one of our *in vivo* systems (*Dictyostelium*) indicates that something more complicated is occurring. Just like for dynein, there must be some factor causing kinesin's stall force to change *in vivo*. Extra *in vivo* regulatory factors that lower kinesin's stall force would be strange as they would be lowering kinesin's efficiency, we know that we are studying the same kinesin *in vivo* and *in vitro* in at least some cases, and from our *in vitro* measurements of kinesin's stall force in hyaluronic acid, we know that viscoelasticity's effect on kinesin's stall force appears to be negligible. These points lead to the idea that perhaps kinesin-dynein interactions through the cargo are what are causing this difference in *in vivo* and *in vitro* stall force.

### **Section 4.3: Synergistic Model**

We believe that the smaller peak is not a kinesin stall peak in itself, but is primarily due to dynein being dragged along behind the kinesin (a theory recently proposed in a manuscript in submission by Dr. Melinda Hoffman from our lab, referred to as the synergistic model). Support for this theory also comes from our *in vitro* dynein and kinesin coated bead data, in which the plus-end directed stall force histogram looks very similar to our *in vivo* anterograde stall force histograms, with the major difference being the small *in vitro* stall force peak is between 1-2 pN, not 2-3 pN as with the *in vivo* measurements (figure 23). As our *in vitro* data consists of nothing but a polystyrene bead with dynein and kinesin on it, and as beads with just kinesin show the

standard *in vitro* kinesin stall force, only the dynein could be causing the change in stall behavior.

This theory is also supported by data in Dr. Hoffman's manuscript taken on the optical trap, where dynein coated beads are pulled backwards, and instead of releasing and getting pulled back to the center of the trap, they will slowly step backwards if pulled backward with forces greater than the stall force. This leads to a model where a kinesin is walking, and pulling along 1-2 dyneins, and because the dyneins impose a minus-end directed force on the plus-end directed motor, the stall force of kinesin would effectively decrease by the stall force of the dynein motors, -2 pN for 1, -4 pN for 2 dyneins (figure 24). This appears most clearly in the A549 anterograde data, but due to variability in stall forces, can still easily explain the *Dictyostelium* and *in vitro* data. Pauses in motion could be caused by three or four dynein motors opposing a single kinesin, by roadblocks such as Microtubule Associated Proteins (MAPs), or other factors, and switching would be caused by roadblocks or stochastic motor binding and unbinding events.

The usefulness of the synergistic model can be seen when the differing characteristics of the two main molecular motors are taken into account. Kinesin rarely reverses under backward force, almost never takes sideways steps on a microtubule (it generally stays on the same protofilament) and detaches when it runs into MAPs, while dynein does reverse fairly easily under backward force, it sidesteps fairly routinely, is thought to have a variable step size, and is less likely to detach when it runs into MAPs. If kinesin runs into some sort of roadblock on the path, it is more or less stuck, and will detach, but if it has been dragging dynein behind it, the dynein will activate, back up, and sidestep around the roadblock (this happens stochastically, so

it might take a few cycles to pass the roadblock). If dynein runs into a roadblock, kinesin can move it backwards and let it have another attempt at passing the blockage.

Finally, our stall force measurements reveal an interesting picture for motor copy number that doesn't appear entirely consistent with our synergistic model. It appears that a majority of the time organelles have one kinesin or one dynein active, not the large groups of motors typically hypothesized. This is particularly interesting for the tug of war model as if there is typically only one active dynein with a significantly lower stall force than kinesin, it seems unlikely it could overwhelm the kinesin in a tug of war. It is also interesting in terms of our synergistic model, in that in our anterograde stall force histograms there appear to be a significant number of motors dragging more than one dynein behind them, but there are almost no retrograde stalls with more than one dynein taking part (figure 24). It also appears force doesn't play as central a role in directional switching as other regulatory measures, motor on/off rates, and microtubule modifications such as MAPs. However the fact that our *in vitro* measurements with both kinesin and dynein on the bead had a similar stall force histogram to the *in vivo* measurements indicates that dynein is the cause of the lowered kinesin stall force *in vivo*. Perhaps dynein being dragged backwards doesn't directly subtract its stall force from kinesin's, but alters the stall force in some other way. This would make some sense as dragging a dynein backwards could take more force than simply stalling it.

## Section 4.4: Figures

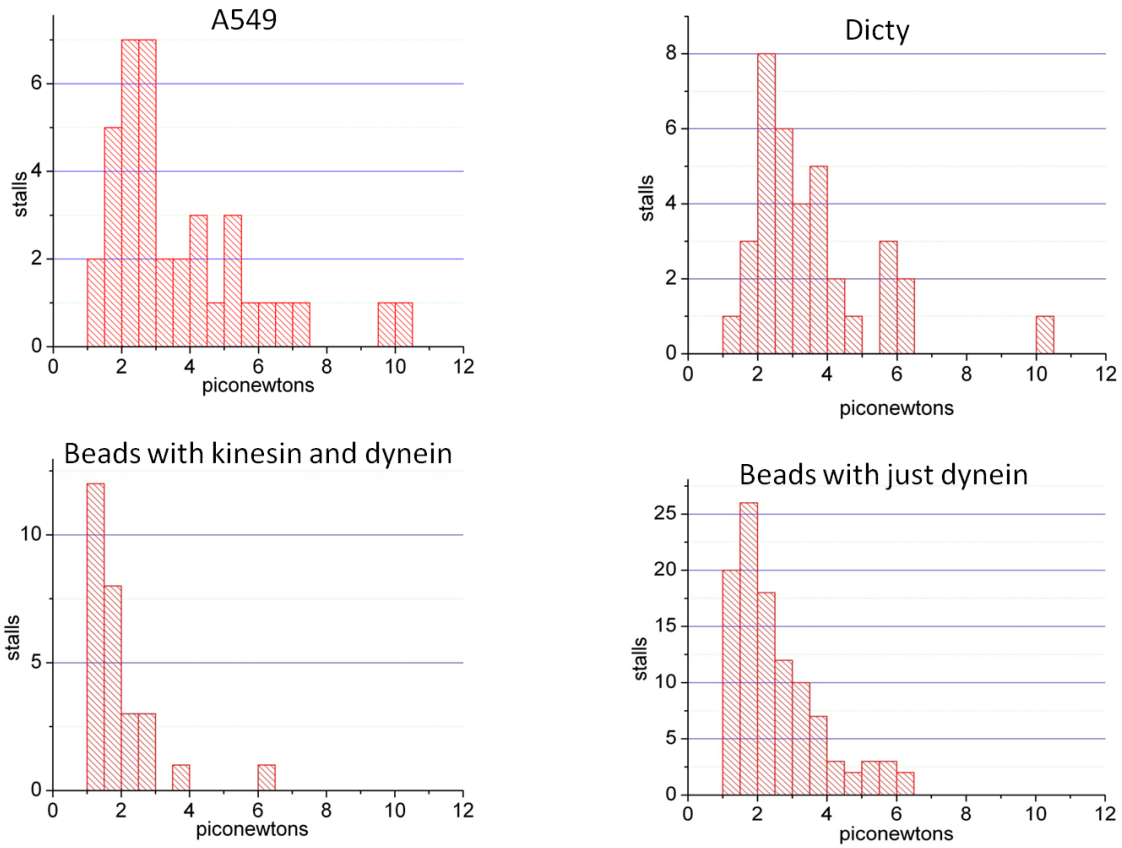


Figure 22: Comparison of Dynein Stalls. These four histograms compare minus-end stalls under different conditions. There is not a significant peak under 2 pN for the *in vivo* data, but both *in vitro* histograms show a stall peak under 2 pN. The beads with only dynein were made with a surplus of dynein to see if we could replicate the *in vivo* histograms, but even with a large number of active dynein the largest peak was still under 2 pN.

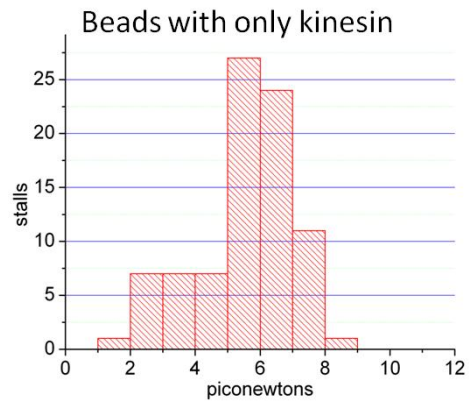
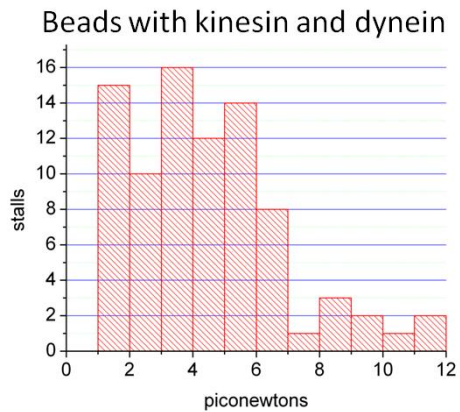
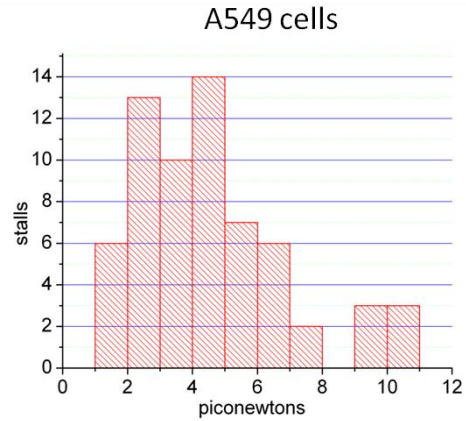
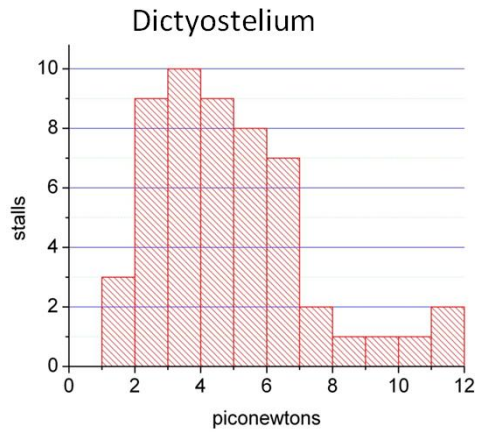


Figure 23: Comparison of Kinesin Stalls: These figures are all plus-end or anterograde directed stalls. Comparing the 4 histograms we can see that the 2 *in vivo* histograms and the kinesin and dynein bead histogram look similar, while the kinesin alone histogram only has a peak between 5-7 pN, indicating that only the motors alone are necessary to explain the different stall forces measured *in vivo*.

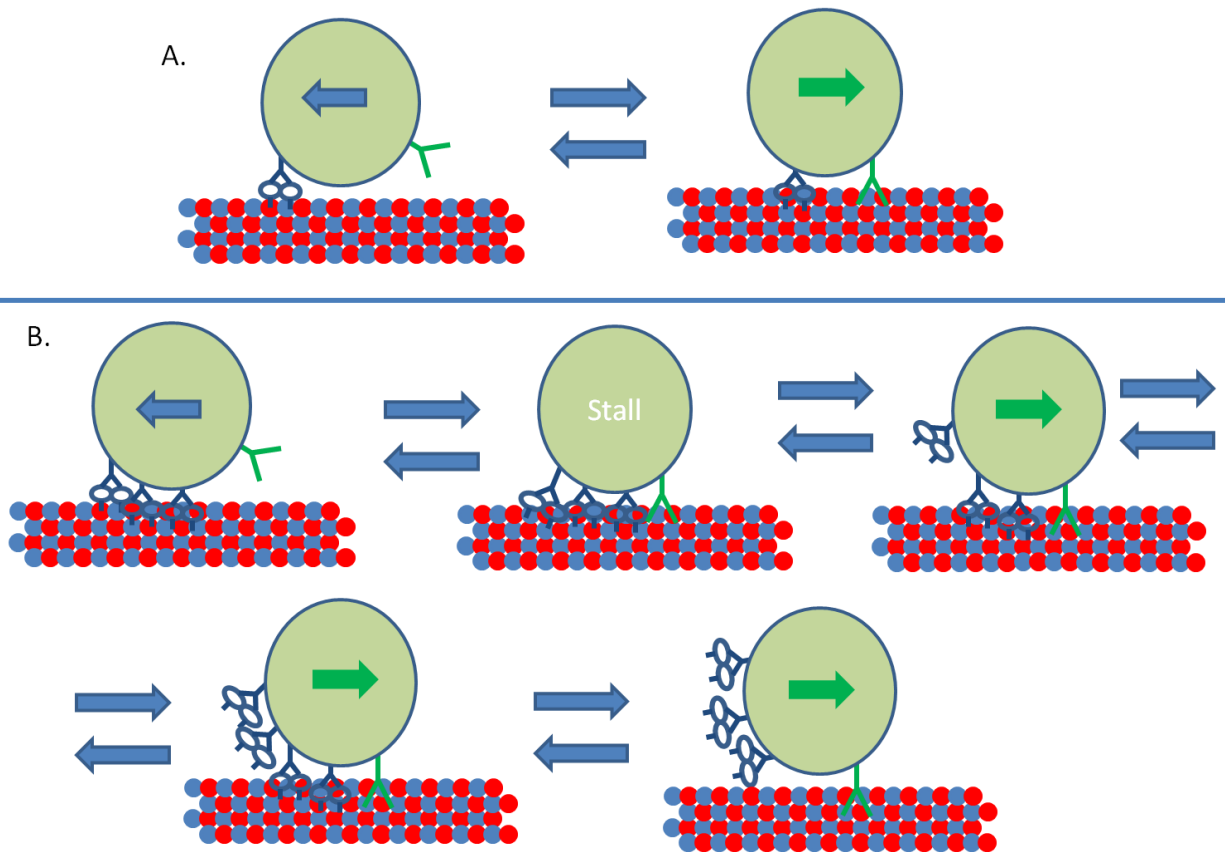


Figure 24: The Synergistic Model. Diagrams showing the various states a cargo can be in within the synergistic model. The arrows on the cargo indicate cargo directionality, and the green motor is kinesin, the blue, dynein.

A. The one dynein version. As our data appear to support there only being one dynein, this is how the synergistic model would act in such a situation. The single dynein would remain attached, while the kinesin's on/off state would determine the directionality of the cargo. Stalling would only occur at obstacles and would never be caused by a tug of war.

B. The multiple dynein version. In this model stalling could occur due to a tug of war between the multiple dynein and the single kinesin, and once again directionality would be determined by the on/off state of the kinesin.

## Chapter 5: Conclusions

We successfully built an optical trap with high speed laser positioning and implemented the fluctuation dissipation technique to measure stall forces in living cells. This allowed us to accurately measure the stall forces of lipid droplets in A549 cells and phagosomes in *Dictyostelium* cells. The anterograde stall forces were measured as 2-3 pN and 4-5 pN in A549 cells and 2-6 pN in *Dictyostelium*, while retrograde stall forces were 2-3 pN in both cell types. We also measured the stall force of full-length conventional kinesin in hyaluronic acid solutions of varying viscoelasticities, showing that high viscoelasticity has negligible effect on kinesin's stall force. Phagosomes were then purified from *Dictyostelium* and stall force measurements on them revealed that the kinesin motor on the phagosomes has a typical *in vitro* kinesin stall force of 6 pN, showing that an unusual motor is not the cause of the differing *in vivo* and *in vitro* stall force. Measurements were then made *in vitro* on beads coated with both kinesin and dynein revealing that the stall force differences between *in vitro* and *in vivo* kinesin can be explained mostly by motor interactions mediated by forces transmitted through the cargo to which both motors are attached.

Although there are still some questions about motor copy number *in vivo*, these results appear to most easily be explained by the recently proposed synergistic model. This model hypothesizes that dynein typically remains attached to the microtubule when kinesin is walking, while kinesin detaches entirely when dynein is walking. This allows dynein to take over cargo transport when kinesin hits an impediment and detaches, or kinesin to pull dynein away from an impediment, in both cases enabling dynein to sidestep around the impediments. This model is suggested by the fact that dynein will step backwards under superstall forces, and that *in vitro* dynein reduces the stall force of kinesin when both are attached to the same cargo.

## **Section 5.1: Future Work**

Purification and stall force measurement on organelles purified from our two *in vivo* systems still remains a high priority. Getting plus-end and minus-end measurements from purified organelles with both motors attached, and each motor attached individually, would allow comparison of the actual *in vivo* motors to their behavior *in vitro* in various situations. This would also allow an accurate motor count on the number of dyneins on the organelles that could be active at once.

## References

1. Vale, R.D., *The molecular motor toolbox for intracellular transport*. Cell, 2003. **112**(4): p. 467-80.
2. Schliwa, M. and G. Woehlke, *Molecular motors*. Nature, 2003. **422**(6933): p. 759-65.
3. Vale, R.D., et al., *Direct observation of single kinesin molecules moving along microtubules*. Nature, 1996. **380**(6573): p. 451-3.
4. Kuo, S.C. and M.P. Sheetz, *Force of single kinesin molecules measured with optical tweezers*. Science, 1993. **260**(5105): p. 232-4.
5. Schnitzer, M.J. and S.M. Block, *Kinesin hydrolyses one ATP per 8-nm step*. Nature, 1997. **388**(6640): p. 386-90.
6. Yildiz, A., et al., *Kinesin walks hand-over-hand*. Science, 2004. **303**(5658): p. 676-8.
7. Svoboda, K. and S.M. Block, *Force and velocity measured for single kinesin molecules*. Cell, 1994. **77**(5): p. 773-84.
8. Mallik, R., et al., *Cytoplasmic dynein functions as a gear in response to load*. Nature, 2004. **427**(6975): p. 649-52.
9. Gennerich, A., et al., *Force-induced bidirectional stepping of cytoplasmic dynein*. Cell, 2007. **131**(5): p. 952-65.
10. Mallik, R., et al., *Building complexity: an in vitro study of cytoplasmic dynein with in vivo implications*. Curr Biol, 2005. **15**(23): p. 2075-85.
11. Ross, J.L., et al., *Processive bidirectional motion of dynein-dynactin complexes in vitro*. Nat Cell Biol, 2006. **8**(6): p. 562-70.
12. Asai, D.J. and M.P. Koonce, *The dynein heavy chain: structure, mechanics and evolution*. Trends Cell Biol, 2001. **11**(5): p. 196-202.
13. Cappello, G., et al., *Myosin V stepping mechanism*. Proc Natl Acad Sci U S A, 2007. **104**(39): p. 15328-33.
14. Yildiz, A., et al., *Myosin V walks hand-over-hand: single fluorophore imaging with 1.5-nm localization*. Science, 2003. **300**(5628): p. 2061-5.
15. Rock, R.S., et al., *Myosin VI is a processive motor with a large step size*. Proc Natl Acad Sci U S A, 2001. **98**(24): p. 13655-9.
16. Neuman, K.C. and S.M. Block, *Optical trapping*. Rev Sci Instrum, 2004. **75**(9): p. 2787-809.
17. Gittes, F. and C.F. Schmidt, *Interference model for back-focal-plane displacement detection in optical tweezers*. Opt Lett, 1998. **23**(1): p. 7-9.
18. Ashkin, A., *Acceleration and Trapping of Particles by Radiation Pressure*. Physical Review Letters, 1970. **24**(4): p. 156-&.
19. Shtridelman, Y., et al., *In vivo Multimotor Force-Velocity Curves by Tracking and Sizing Sub-Diffraction Limited Vesicles*. Cellular and Molecular Bioengineering, 2009. **2**(2): p. 190-199.
20. Mizuno, D., et al., *Nonequilibrium mechanics of active cytoskeletal networks*. Science, 2007. **315**(5810): p. 370-3.
21. Shubeita, G.T., et al., *Consequences of motor copy number on the intracellular transport of kinesin-1-driven lipid droplets*. Cell, 2008. **135**(6): p. 1098-107.
22. Sims, P.A. and X.S. Xie, *Probing dynein and kinesin stepping with mechanical manipulation in a living cell*. Chemphyschem, 2009. **10**(9-10): p. 1511-6.

23. Fischer, M., et al., *Active-passive calibration of optical tweezers in viscoelastic media*. Rev Sci Instrum. **81**(1): p. 015103.
24. Fischer, M. and K. Berg-Sorensen, *Calibration of trapping force and response function of optical tweezers in viscoelastic media*. Journal of Optics a-Pure and Applied Optics, 2007. **9**(8): p. S239-S250.
25. Heidemann, S.R. and D. Wirtz, *Towards a regional approach to cell mechanics*. Trends Cell Biol, 2004. **14**(4): p. 160-6.
26. Jolly, A.L. and V.I. Gelfand, *Bidirectional intracellular transport: utility and mechanism*. Biochem Soc Trans. **39**(5): p. 1126-30.
27. Spudich, J.A., *Molecular motors: forty years of interdisciplinary research*. Mol Biol Cell. **22**(21): p. 3936-9.
28. Rebhun, L.I., *Structural aspects of saltatory particle movement*. J Gen Physiol, 1967. **50**(6): p. Suppl:223-39.
29. Gross, S.P., et al., *Coordination of opposite-polarity microtubule motors*. J Cell Biol, 2002. **156**(4): p. 715-24.
30. Martin, M., et al., *Cytoplasmic dynein, the dynactin complex, and kinesin are interdependent and essential for fast axonal transport*. Mol Biol Cell, 1999. **10**(11): p. 3717-28.
31. Muller, M.J., S. Klumpp, and R. Lipowsky, *Bidirectional transport by molecular motors: enhanced processivity and response to external forces*. Biophys J. **98**(11): p. 2610-8.
32. Muller, M.J., S. Klumpp, and R. Lipowsky, *Tug-of-war as a cooperative mechanism for bidirectional cargo transport by molecular motors*. Proc Natl Acad Sci U S A, 2008. **105**(12): p. 4609-14.
33. Welte, M.A., *Bidirectional transport along microtubules*. Curr Biol, 2004. **14**(13): p. R525-37.
34. Laib, J.A., et al., *The reciprocal coordination and mechanics of molecular motors in living cells*. Proc Natl Acad Sci U S A, 2009. **106**(9): p. 3190-5.
35. Pollock, N., et al., *In vitro microtubule-based organelle transport in wild-type Dictyostelium and cells overexpressing a truncated dynein heavy chain*. Cell Motil Cytoskeleton, 1998. **40**(3): p. 304-14.
36. Klopfenstein, D.R., E.A. Holleran, and R.D. Vale, *Kinesin motors and microtubule-based organelle transport in Dictyostelium discoideum*. J Muscle Res Cell Motil, 2002. **23**(7-8): p. 631-8.
37. Pollock, N., et al., *Reconstitution of membrane transport powered by a novel dimeric kinesin motor of the Unc104/KIF1A family purified from Dictyostelium*. J Cell Biol, 1999. **147**(3): p. 493-506.
38. Ashkin, A., et al., *Force generation of organelle transport measured in vivo by an infrared laser trap*. Nature, 1990. **348**(6299): p. 346-8.
39. Soppina, V., et al., *Tug-of-war between dissimilar teams of microtubule motors regulates transport and fission of endosomes*. Proc Natl Acad Sci U S A, 2009. **106**(46): p. 19381-6.
40. Lu, H., et al., *Diffusive movement of processive kinesin-1 on microtubules*. Traffic, 2009. **10**(10): p. 1429-38.
41. Bingham, J.B., S.J. King, and T.A. Schroer, *Purification of dynactin and dynein from brain tissue*. Methods Enzymol, 1998. **298**: p. 171-84.

42. Pierce, D.W. and R.D. Vale, *Assaying processive movement of kinesin by fluorescence microscopy*. *Methods Enzymol*, 1998. **298**: p. 154-71.
43. Brouhard, G.J., H.T. Schek, 3rd, and A.J. Hunt, *Advanced optical tweezers for the study of cellular and molecular biomechanics*. *IEEE Trans Biomed Eng*, 2003. **50**(1): p. 121-5.
44. Lang, M.J., et al., *An automated two-dimensional optical force clamp for single molecule studies*. *Biophys J*, 2002. **83**(1): p. 491-501.
45. Tolic-Norrelykke, S.F., et al., *Calibration of optical tweezers with positional detection in the back focal plane*. *Review of Scientific Instruments*, 2006. **77**(10).
46. Berg-Sorensen, K. and H. Flyvbjerg, *Power spectrum analysis for optical tweezers*. *Review of Scientific Instruments*, 2004. **75**(3): p. 594-612.
47. Fukui, Y., S. Yumura, and T.K. Yumura, *Agar-overlay immunofluorescence: high-resolution studies of cytoskeletal components and their changes during chemotaxis*. *Methods Cell Biol*, 1987. **28**: p. 347-56.
48. Nijenhuis, N., et al., *Microrheology of hyaluronan solutions: implications for the endothelial glycocalyx*. *Biomacromolecules*, 2008. **9**(9): p. 2390-8.
49. Toba, S., et al., *Overlapping hand-over-hand mechanism of single molecular motility of cytoplasmic dynein*. *Proc Natl Acad Sci U S A*, 2006. **103**(15): p. 5741-5.

# Appendix

## A.1 *In Vitro* Stall Picking Program

```
%This program goes through a long position trace section by section and
%asks if there is a stall. If you respond yes, you get to select by
%brushing over the bottom and top of the stall, and then the program will
%calculate the stall force, put it in a list, and move on. The output is
%the list of stall forces.
clear %closes any open variables in the workspace
close all%closes all open figures
[FileName,PathName,FilterIndex]=uigetfile({'*.*','All Files
(*.*)'},'MultiSelect','on');
FileName = cellstr(FileName);
A=size(FileName);
A=A(2); %A is a 1x2 array, I need the second column.
datarate = input('enter data acquisition rate in Hz');
beta = input('enter beta in nm/V');
stiff = input('enter trap stiffness in pN/nm');
steta= beta*stiff;
D=2; %this specifies the dimension of motion (right now it is X, 3 is Y)
for k=1:A
    %try %this catches errors and moves on to the next k value if one is
    %found.
    B=char(strcat(PathName,FileName(k)))
    C=10; %this is the amount to smooth
    XYS = dlmread(B, '\t');
    scans=size(XYS,1);
    XY=zeros(scans,2);
    XY(:,1) = steta*XYS(:,1)./XYS(:,3);
    XY(:,2) = steta*XYS(:,2)./XYS(:,3);
    XY(:,1) = smooth(XY(:,1),C);
    XY(:,2) = smooth(XY(:,2),C);
    T=transpose(0:(1/datarate):((scans-1)/datarate));
    Tlength=scans/datarate;
    TXY=cat(2, T, XY);
    figure(2);
    plot(TXY(:,1),TXY(:,D));% this is assuming that all the motion is
%occurring in the x direction.
    numseg = ceil(Tlength/10); %number of 10 sec segments
    forces=[];
    for i=1:numseg;
        if i == numseg %this picks out the last section which might be
%less than 10 sec long
            ma=max(TXY(((i-1)*datarate*10+1):Tlength*datarate,D)); %this
%picks out min and max to set Y-axis values
            mi=min(TXY(((i-1)*datarate*10+1):Tlength*datarate,D));
            TXYshort=TXY(datarate*(i-1)*10+1:datarate*Tlength,:);
        else
            TXYshort=TXY(datarate*(i-1)*10+1:datarate*i*10,:);
            ma=max(TXY(((i-1)*datarate*10+1):(i*datarate*10),D));
            mi=min(TXY(((i-1)*datarate*10+1):(i*datarate*10),D));
        end
        figure(1);
        plot(TXYshort(:,1),TXYshort(:,D));
        grid on;
```

```

grid minor;
set(gca, 'XTick', (i-1)*10:.5:(i*10));
axis ([(i-1)*10,i*10,mi,ma]);
stall=menu('Is there a stall in this plot?','yes','no');
while stall == 1
    %%this section selects the upper and lower parts of the stall,
    %%then calculates the stall force and asks if there is
    %%another stall.
    brush on
    h=brush;
    pause
    hBrushLine = findall(gca, 'tag', 'Brushing'); %these four lines I
%stole from a website tutorial on how to access
    brushedData = get(hBrushLine, {'Xdata', 'Ydata'}); %brushed data
%programatically. the website is undocumented matlab.com/blog/accessing-
%plot-brushed-data/
    brushedIdx = ~isnan(brushedData{1}); %it some how finds a line in
%uiinspect that stores the brushed data info, and
    brushedYData = brushedData{2}(brushedIdx); % then we just have to
%remove the NaN (everything not selected).
    s1=mean(brushedYData);
    clear hBrushLine;
    brush off;
    %after removing the old figure I reopen the same plot and find
    %the second half of the stall.
    figure(1);
    plot(TXYshort(:,1),TXYshort(:,D));
    axis ([(i-1)*10,i*10,mi,ma]);
    grid on;
    grid minor;
    set(gca, 'XTick', (i-1)*10:.5:(i*10));
    brush on
    q=brush;
    pause
    qBrushLine = findall(gca, 'tag', 'Brushing'); %these four lines I
%stole from a website tutorial on how to access
    brushedData = get(qBrushLine, {'Xdata', 'Ydata'}); %brushed data
%programatically. the website is undocumented matlab.com/blog/accessing-
%plot-brushed-data/
    brushedIdx = ~isnan(brushedData{1}); %it some how finds a line in
%uiinspect that stores the brushed data info, and
    brushedYData = brushedData{2}(brushedIdx); % then we just have to
%remove the NaN (everything not selected).
    s2=mean(brushedYData);
    brush off;
    stot=abs(s1-s2)
    forces=cat(1, forces, stot);
    figure(1);
    plot(TXYshort(:,1),TXYshort(:,D));
    axis ([(i-1)*10,i*10,mi,ma]);
    grid on;
    grid minor;
    set(gca, 'XTick', (i-1)*10:.5:(i*10));
    stall=menu('Is there a stall in this plot?','yes','no');
end
end
F=regexprep(B, '.txt', '_stalls.txt');

```

```

        dlmwrite(F, forces, '\t');
    %catch exception
        %continue
    %end
end

```

## A.2 *In Vivo* Stall Picking Program

This program is similar to the *in vitro* stall picking program, in that you scroll through and pick out stalls. It gives you comparison graphs between the CCD and QPD position data also, to check for errors.

```

%this program wants you to choose the filtered down files, assumes camera
%data of 180 frames and calls the function stallbrush. It requires you to
%have run the Pulse Analysis program, and to have run FIONA on your CCD
%video of the trapped cargo.
clear %closes any open variables in the workspace
close all%closes all open figures
[FileName, PathName, FilterIndex]=uigetfile({'*.*', 'All Files
(*.*)'}, 'MultiSelect', 'on');
FileName = cellstr(FileName);
A=size(FileName);
A=A(2); %A is a 1x2 array, I need the second column.
stiffratio=1; % this is to correct for x and y having different stiffnesses
%it is X/Y
forces=[]; %this is where I will store the measured force for every file and
%print it out later
for k=1:A
    B=char(strcat(PathName, FileName(k))); %this is the filtered down data
    FileName(k)
    C=10; %this is the amount to smooth
    XYS = dlmread(B, '\t');
    B2=regexprep(B, '_filter.txt', '_test.txt');
    stiff=dlmread(B2, '\t', 'L1..L1');
    scans=size(XYS,1);
    TXY=zeros(scans,3);
    xm=mean(XYS(:,2));
    ym=mean(XYS(:,3));
    TXY(:,2) = stiff.*(XYS(:,2)-xm).*stiffratio;
    TXY(:,3) = stiff.*(XYS(:,3)-ym);
    TXY(:,2) = smooth(TXY(:,2),C);
    TXY(:,3) = smooth(TXY(:,3),C);
    TXY(:,1) = XYS(:,1);
    L=TXY(2,1)*(scans-1);
    C=regexprep(B, '0_filter.txt', 'CAMERA.tif.csv'); %replace part of a
%string
    cXY=dlmread(C, ',', 'E1..F180');%this loads the camera position data in
%pixels, assumes camera data is 180 frames long
    cXY=cXY.*(-177.78).*stiff;%177.78nm is the pixel size of the camera
    cXY(:,1)=(cXY(:,1)-mean(cXY(:,1))).*stiffratio;%recentering around zero
    cXY(:,2)=cXY(:,2)-mean(cXY(:,2));
    cT=(0:1:179)./24';%this will be a known amount with the new data, so
%change this later
    figure(1);
    plot(TXY(:,1), TXY(:,2), TXY(:,1), TXY(:,3), cT, cXY(:,1), cT, cXY(:,2));
    pause;
    grid on;

```

```

grid minor;
set(gca,'XTick',0:.5:L);
figure(1);
plot(TXY(:,1),TXY(:,2),TXY(:,1),TXY(:,3));
grid on;
grid minor;
set(gca,'XTick',0:.5:L);
stall=menu('Is there a stall in these plots?', 'x', 'y','both', 'no');
while (stall < 4)
    if (stall < 3)
        d=stall+1;
        stot=stallbrush(TXY,d,L);
        stot
        forces=cat(1,forces,stot);
    elseif (stall == 3)
        d=2;
        stot=stallbrush(TXY,d,L);
        xstiff=stot;
        d=3;
        stot=stallbrush(TXY,d,L);
        ystiff=stot;
        stot=sqrt(ystiff^2+xstiff^2);
        stot
        forces=cat(1,forces,stot);
    end
    figure(1);
    plot(TXY(:,1),TXY(:,2),TXY(:,1),TXY(:,3));
    grid on;
    grid minor;
    set(gca,'XTick',0:.5:L);
    stall=menu('Is there another stall in these plots?', 'x', 'y','both',
'no');
end
end
F=regexprep(B, '_filter.txt', '_stalls.txt');
dlmwrite(F, forces, '\t');

```

## Filter Down Program

This program filters down the raw *in vivo* position data to allow for easier analysis.

```

%Choose the raw position files from in vivo trap data. This will filter
%them down to 4000 Hz and 400Hz data from 80 kHz.
clear %closes any open variables in the workspace
close all%closes all open figures
[FileName,PathName,FilterIndex]=uigetfile({'*.*','All Files
(*.*)'}, 'MultiSelect', 'on');
FileName = cellstr(FileName);
A=size(FileName);
A=A(2); %A is a 1x2 array, I need the second column.
%scans = input('enter number of scans');
cutlist=[];
for k=1:A
    %try %this catches errors and moves on to the next k value if one is
%found.
    B=char(strcat(PathName,FileName(k)));
    %C=sprintf('%d',scans);

```

```

        %D=strcat('A1..D',C); %this picks the 4 columns T, X, Y, sum for
%analysis.
    % need to change for different versions of the program, as their
%column positions change.
    XYS = dlmread(B, '\t');
    scans=size(XYS,1);
    T = XYS(:,1);
    XY(:,1) = XYS(:,2)./XYS(:,4);
    XY(:,2) = XYS(:,3)./XYS(:,4);
    XY(:,1) = XY(:,1)-mean(XY(:,1));
    XY(:,2) = XY(:,2)-mean(XY(:,2));
    XYshort=zeros((scans/20),2);
    XYtiny=zeros((scans/20),2); %this is necessary to have zeroes filling
%out the back end of the column or I won't
    Ttiny=zeros((scans/20),1);% be able to concatenate all 4 columns at
%the end
    Tshort=T(1:20:scans);
    Ttiny(1:scans/200)=T(1:200:scans); %this leaves the extra zeroes for
%concatentation
    for i=1:(scans/20)
        XYshort(i,:)=mean(XY(((i-1)*20+1):i*20,:),1);
    end
    for i=1:(scans/200)
        XYtiny(i,:)=mean(XY(((i-1)*200+1):i*200,:),1);
    end
    G=regexprep(B, '.txt', '_AOM.txt'); %replace part of a string
    beta=dlmread(G, '\t', 'F2..F2');
    XYshort=XYshort.*beta;
    XYtiny=XYtiny.*beta;
    TXYshort=cat(2,Tshort, XYshort, Ttiny, XYtiny);
    F=regexprep(B, '.txt', '_filter.txt');
    dlmwrite(F, TXYshort, '\t');
    %catch exception
    %continue
%end
end

```

### A.3 *In Vivo* Calibration

```

%this program takes raw position data, beta, and info about the data
%acquisition and analyzes it using the method in "Calibration of Trapping
%Force and Response Function of Optical Tweezers in Viscoelastic Media." It
%calls the function StiffFitFunc.
%%this initial section selects and loads the files I want to analyze.
%%Select the raw position data files you wish to analyze.
clear;
close all;
[FileName, PathName, FilterIndex]=uigetfile({'*.*', 'All Files
(*.*)'}, 'MultiSelect', 'on');
FileName=cellstr(FileName);
A=size(FileName);
A=A(2);
avg=10; %number of times to average down
sAll=[];
betaAll=[];
for k=1:A
    %%this section loads the data and selects the data for sectioning. %%

```

```

    fn=char(strcat(PathName,FileName(k))); %creates a filename string, and
%converts it to char.
    data=dlmread(fn, '\t'); %reads in the raw position data

data=[data(:,2)./data(:,4),data(:,3)./data(:,4),data(:,5)./data(:,7),data(:,6)
)./data(:,7)];
    fn1=regexprep(fn, '.txt', 'info.txt');
    fn2=regexprep(fn, '.txt', '_AOM.txt');
    pf=dlmread(fn1, '\t', 'A5..A47');%this stores data acquisition info
%pf=[pulse freq, time length
%of the entire scan, and scan period (active and passive
%cycle together), OscAmps, OscFreqs]
    OscFreq=pf(24:43);
    OscAmp=pf(4:23);
    beta=dlmread(fn2, '\t', 'F2..F2');
    betaAll=cat(1,betaAll,beta);
    S=floor(1/(2*pf(3)*pf(1))); % # scans per half pulse (aka the number of
%scans in the active or passive part of a pulse)
    B=floor(pf(1)*pf(2))*2-1; %number of iterations to take (# pulses*2-1, to
%get every half second measurement).
    F=size(OscFreq,1);
    A=size(data(1:S,:));
    K=zeros(F,1);
    output=zeros(F*B,7);
    V=zeros(B*F,2);
    V1=zeros(B*F,2);
    St=zeros(B*F,1);
    for i=1:B
        %%%section 1%%
        %This initial section takes the FFT and power spectrums of the two
%segments
        %of each scan.
        h=floor(i/2)*2*S;
        hh=(floor((i-1)/2)*2+1)*S;
        V(i,:)=var(data(hh+1:hh+S,1:2));
        %this part cuts the data into ten pieces, takes the FFT, and then
%averages it to get higher accuracy at the frequencies I want.
        FTdata=zeros(A(1)/avg,2);%creating matrices to store values
        PS=zeros(A(1)/avg,1);
        Y=zeros(A(1)/avg,1);
        for j=1:avg
            %I subtract away the means here so that the FFTs don't have a
%huge fake dc component.
            datmean1=mean(data((j-1)*S/avg+h+1:S/avg*j+h,:));
            FTdata1=(fft(data((j-1)*S/avg+h+1:S/avg*j+h,2)-
datmean1(2))./4000);
            FTdata1(2:S/(2*avg))=FTdata1(2:S/(2*avg)).*2;%this converts to a
%single sided spectrum
            FTdata2=(fft(data((j-1)*S/avg+h+1:S/avg*j+h,4)-
datmean1(4))./4000);
            FTdata2(2:S/(2*avg))=FTdata2(2:S/(2*avg)).*2;
            FTdata1=cat(2,FTdata1,FTdata2);
            FTdata=FTdata+FTdata1;
            datmean2=mean(data(S/avg*(j-1)+hh+1:S/avg*j+hh,2));
            Z=fft(data(S/avg*(j-1)+hh+1:S/avg*j+hh,2)-datmean2);
            Y1=(abs(Z)./4000);
            Y=Y1+Y;

```

```

        PS1=(Y1./sqrt(2)).^2); %This creates the power spectrum. I
%divide by the square root of 2
        %because I need rms values to equalize the sum of the power
        %spectrum and the variance of the data set.
        PS1=PS1./(pf(1)*avg*2); %This creates the PSD (the power spectrum
%divided by the frequency spacing).
        PS1(2:S/avg)=PS1(2:S/avg).*2;%this makes the power spectrum
%single sided.
        PS=PS+PS1;
    end
    FTdata=FTdata./avg;
    PS=PS./avg;
    mag=abs(FTdata);
    ang=angle(FTdata);
    phase=ang(:,2)-ang(:,1); %relative phase difference between
    %the laser and bead oscillation.
    phase=rem(phase,2*pi);
    %%section 2%%
    %This section will pick out the frequencies I oscillate at, and then
    %compute the stiffness.
    fs=2*pf(1)*avg; %This is the frequency spacing of the FFT and PS
%data.
    kt=4.04;%this is the boltzman constant times temperature in pN*nm
    ReR=zeros(F,1);%These two will be the real and imaginary parts of
    ImR=zeros(F,1);%the active spectrum.
    PSw=zeros(F,1);%These will be the power spectrum values I need.
    phasew=zeros(F,1);
    magw=zeros(F,1);
    for j=1:F
        pos=OscFreq(j)/fs;%goes from frequency to array position.
        pos=pos+1;%this is necessary because DC starts at 1 not 0.
        ReR(j)=(-sin(phase(pos))*mag(pos,1))/(OscFreq(j)*2*pi*OscAmp(j));
        ImR(j)=(-cos(phase(pos))*mag(pos,1))/(OscFreq(j)*2*pi*OscAmp(j));
        PSw(j)=PS(pos);
        phasew(j)=phase(pos)*180/pi;
        magw(j)=mag(pos,1);
    end
    %this is to allow me to average all the stiffnesses.
    K=2*kt.*ReR./(beta.*PSw); %these are the stiffnesses
    output((i-1)*F+1:i*F,1:7)=cat(2,OscFreq, K, ReR, ImR, PSw, magw,
phasew);

    end
    fn3=regexprep(fn, '.txt', '_test.txt')
    V1(1,1:2)=4.04./(beta^2.*mean(V(1:B,:)));
    V1(1,1:2)
    s=StiffFitFunc(output(:,2));
    s
    St(1,1)=s.m;
    output=cat(2,output,V,V1,St);
    dlmwrite(fn3, output, '\t');
    smean=mean(output(:,2));
    smean
    sAll=cat(1,sAll,s.m);
    gcf
end
meanStiff=mean(sAll)

```

```
meanbeta=mean(betaAll)
```

### Sitffness Fitting Function

This is the function called by the *in vivo* calibration program. It fits the stall distribution with an equation from Churchman et al, 2006, “A Non-Gaussian Distribution Quantifies Distances Measured with Fluorescence Localization Techniques”.

```
function [ k ] = StiffFitFunc( stiff )
%StiffFitFunc
%This program will take the stiffness input and fit a function to it to
discover
%the true stiffness. Use
%this for distributions with means close to zero, with large variances,
%that are necessarily positive.
%%section 1%%
%This section kicks out the negative measurements and measurements outside
%of 3 standard deviations.
A=sort(stiff, 'descend');
B=A>0;
D=B.*A;
[~,I]=min(D); %gives the index of the 1st minimum value
pstiff=A(1:I-1);
sds=sqrt(var(pstiff));
E=pstiff>(mean(pstiff)-3*sds);
F=pstiff<(mean(pstiff)+3*sds);
G=sort(pstiff.*E.*F, 'descend');
[~,J]=min(G);
gstiff=G(1:J-1);
%%section 2%%
%this section rearranges the points into histogram format and fits the
%function to them
bs=sds/2; %bin spacing for histogram
hstiff=(hist(gstiff, min(gstiff):bs:max(gstiff)+bs)); %creates hist data
nstiff=hstiff./(bs*sum(hstiff));%normalizes histogram
mg=mean(gstiff);
X=(min(gstiff):bs:max(gstiff)+bs)+sds/4);%creates X data
ffun = fittype('sqrt(2/pi)*1/sd*cosh(m*x/sd^2)*exp(-(m^2+x^2)/(2*sd^2))',...
    'independent','x','coefficients',{'sd','m'});
g=fitoptions('Method','NonlinearLeastSquares','StartPoint',[sds,mg]...
    , 'Lower',[0,mg-2*sds], 'Upper',[10*sds, mg+2*sds], 'MaxIter', 1000,...
    'MaxFunEvals', 1000, 'TolFun', 10^-6, 'TolX', 10^-6);
cfun=fit(X,nstiff,ffun,g);
astiff=(hist(A, min(A):bs:max(A)+bs));
astiff=astiff./(bs*sum(astiff));
X1=min(A):bs:max(A)+bs;
figure
plot(X1,astiff,X,cfun(X));
k=cfun;

end
```

## A.4 Viscoelasticity Analysis

This program will extract the elasticities, viscosities and various other rheological parameters from *in vivo* calibration data, allowing one to look at the change over time of the various parameters, and the change over frequency.

```

%This program is to analyze viscoelasticity data (after April or May 2010
from the new MatLab program) and output G', G'',
%viscosity, elasticity ... pick the _test files from the in vivo calibration
program PulseAnalysis.
clear %closes any open variables in the workspace
close all%closes all open figures
[FileName,PathName,FilterIndex]=uigetfile({'*.*','All Files
(*.*)'},'MultiSelect','on');
FileName = cellstr(FileName);
A=size(FileName);
A=A(2); %A is a 1x2 array, I need the second column.
D=char(strcat(PathName,'VE.txt'));
V1=zeros(20*A,1);
E1=zeros(20*A,1);
rheoave=zeros(260,14);
for k=1:A
    B=char(strcat(PathName,FileName(k)));
    t = dlmread(B, '\t'); %read in the data
    s=size(t);
    G=regexprep(B, '_test.txt', '_AOM.txt'); %replace part of a string
    beta=dlmread(G, '\t', 'F2..F2');
    w=(2.*pi.*t(:,1));
    H=regexprep(B, '_test.txt', '_filter.txt');%replace part of a string
    XYS = dlmread(H, '\t');
    scans=size(XYS,1);
    TXY=zeros(scans,3);
    xm=mean(XYS(:,2));
    ym=mean(XYS(:,3));
    C=10; %this is the amount to smooth
    TXY(:,2) = (XYS(:,2)-xm);
    TXY(:,3) = (XYS(:,3)-ym);
    TXY(:,2) = smooth(TXY(:,2),C);
    TXY(:,3) = smooth(TXY(:,3),C);
    TXY(:,1) = XYS(:,1);
    L=TXY(2,1)*(scans-1);
    %this line is the mass of the trapped object in grams, polystyrene sphere
    %(density 1.05 g/cm-3). R is the radius in nm.
    %m=1.1.*10.^-12; %1.26um polystyrene
    %R=630; %nanometers
    m=1.1.*10.^-12;
    R=630;
    %this line is for the beta volts to nm conversion (pulse cal type)
    BC=1./(w.*t(:,4));
    %these next two lines are the friction relaxation spectrums. units of
    %grams per second.
    fpp=(t(:,2)./w).*((t(:,4)./(w.*beta.*(t(:,3).^2+t(:,4).^2))-1)-w.*m;
    fp=(1./beta).*(t(:,2)./w).*(t(:,3)./(w.*(t(:,3).^2+t(:,4).^2)));
    %These two are the complex modulus. units of pN/nm^2.
    Gp=w./(6.*pi.*R).*fpp;
    Gpp=w./(6.*pi.*R).*fp;
    %now viscosity and elasticity. units of pN*sec/nm^2.
    V=Gpp./w;
    E=Gp./w;
    %Now I will convert everything to SI units (Pascals...)
    V=V.*10.^6;

```

```

E=E.*10.^6;
Gpp=Gpp.*10^6;
Gp=Gp.*10^6;
% now I am rearranging and manipulating the data so I can more easily
% analyze and visualize it.
S=size(V);
pnum=S(1)./20;
%creating the average at every frequency by averaging over time.
Vavg=zeros(S(1),1);
Eavg=zeros(S(1),1);
Gpavg=zeros(S(1),1);
Gppavg=zeros(S(1),1);
for i=1:20
    Vavg(i)=mean(V(i:20:S));
    Eavg(i)=mean(E(i:20:S));
    Gpavg(i)=mean(Gp(i:20:S));
    Gppavg(i)=mean(Gpp(i:20:S));
end
%this averages all the frequencies per pulse, to see if there is a
%change over time.
SS=S(1)/20;
Vchange=zeros(S(1),1);
V1=zeros(SS,1);
V2=zeros(SS,1);
V3=zeros(SS,1);
V4=zeros(SS,1);
Echange=zeros(S(1),1);
E1=zeros(SS,1);
E2=zeros(SS,1);
E3=zeros(SS,1);
E4=zeros(SS,1);
for i=1:pnum
    Vchange(i)=mean(V(((i-1)*20+1):i*20));
    V1(i)=mean(V(((i-1)*20+1):(i-1)*20+3));
    V2(i)=mean(V(((i-1)*20+4):(i-1)*20+8));
    V3(i)=mean(V(((i-1)*20+9):(i-1)*20+14));
    V4(i)=mean(V(((i-1)*20+15):(i-1)*20+20));
    Echange(i)=mean(E(((i-1)*20+1):i*20));
    E1(i)=mean(E(((i-1)*20+1):(i-1)*20+3));
    E2(i)=mean(E(((i-1)*20+4):(i-1)*20+8));
    E3(i)=mean(E(((i-1)*20+9):(i-1)*20+14));
    E4(i)=mean(E(((i-1)*20+15):(i-1)*20+20));
    Xc=1:pnum;
end
time=(.5:.5:6.5);
figure(1);
plot(time,V1,time,V2,time,V3,time,V4);
figure(3);
plot(time,E1,time,E2,time,E3,time,E4);
figure(2);
grid on;
grid minor;
set(gca,'XTick',0:.5:L);
%this next set of lines is plotting everything in the same figure with
%different Y axes, so they are scaled correctly. Got it from the
%matlab help.
line(TXY(:,1),TXY(:,2),'Color','r');%plots x red

```

```

line(TXY(:,1),TXY(:,3),'Color','b');%plots y blue
ax1=gca;
set(ax1,'XColor','r','YColor','r'); %changes axes color

ax2=axes('Position',get(ax1,'Position'),'YAxisLocation','right','Color','none',
'YColor','k');
line(time,Vchange(1:13),'Color','k');
line(time,Echange(1:13),'Color','green');
C=regexprep(B, '_test.txt', '_VE.txt'); %replace part of a string

rheo=[t(:,1),V,E,Gp,Gpp,fp,fpp,Vavg,Eavg,Vchange,Echange,Gpavg,Gppavg,BC];
dlmwrite(C, rheo, '\t');
rheoave=rheoave+rheo;
end
rheoave=rheoave./A;
J=regexprep(B, '_test.txt', '_VEave.txt'); %replace part of a string
dlmwrite(J, rheoave, '\t');

```